nature communications

Article

https://doi.org/10.1038/s41467-025-57570-7

Different fibroblast subtypes propel spatially defined ileal inflammation through TNFR1 signalling in murine ileitis

Received: 5 March 2024

Accepted: 25 February 2025

Published online: 28 March 2025

Check for updates

Lida Iliopoulou[1,5], Christos Tzaferis[1,5], Alejandro Prados[1,4,5], Fani Roumelioti[1], Vasiliki Koliaraki[2] & George Kollias[1,3]

Crohn's disease (CD) is a persistent inflammatory disorder primarily affecting the terminal ileum. The $Tnf^{\Delta ARE}$ mice, which spontaneously develop CD-like ileitis due to TNF overexpression, represent a faithful model of the human disease. Here, via single-cell RNA sequencing in $Tnf^{\Delta ARE}$ mice, we show that murine TNF-dependent ileitis is characterized by cell expansion in tertiary lymphoid organs (TLO), T cell effector reprogramming, and accumulation of activated macrophages in the submucosal granulomas. Within the stromal cell compartment, fibroblast subsets (telocytes, trophocytes, $Pdgfra^{lo}Cd81^{-}$ cells) are less abundant while lymphatic endothelial cells (LEC) and fibroblastic reticular cells (FRC) show relative expansion compared to the wild type. All three fibroblast subsets show strong pro-inflammatory signature. TNFR1 loss or gain of function experiments in specific fibroblast subsets suggest that the $Tnf^{\Delta ARE}$-induced ileitis is initiated in the lamina propria via TNF pathway activation in villus-associated fibroblasts (telocytes and $Pdgfra^{lo}Cd81^{-}$ cells), which are responsible for the organization of TLOs. Trophocytes drive disease progression in the submucosal layer, accompanied by the excessive formation of granulomas. These findings provide evidence for spatial regulation of inflammation by fibroblast subsets and underscore the pivotal role of fibroblasts in the inception and advancement of ileitis.

Inflammatory Bowel Disease (IBD) comprises two primary clinical subtypes, namely Crohn's disease (CD) and Ulcerative Colitis (UC). Both subtypes involve the development of chronic inflammation in the gastrointestinal tract, but differ in their underlying mechanisms and sites of manifestation[1,2]. CD primarily affects the terminal ileum, whereas UC is localized to the colon[2]. Furthermore, in CD, there is frequently an infiltration of immune cells into the deeper layers of the intestinal wall, including the submucosa and muscularis mucosa, often accompanied by the clustering of macrophages within granulomas[3].

Tumor necrosis factor (TNF) plays a significant pathogenic role in the development and progression of IBD, as evidenced by the successful use of anti-TNF therapy in IBD patients for over 30 years in clinical practice[4,5]. $Tnf^{\Delta ARE}$ mice, which spontaneously develop CD-like ileitis due to TNF overexpression[6], have proven to be a valuable platform for elucidating TNF-dependent mechanisms over the years[7].

Various intestinal stroma and immune cell types actively participate in the progression of CD[8,9]. Leveraging the capabilities of single-cell RNA sequencing (scRNA-seq) methodologies, several studies have provided insights into the cellular heterogeneity within the inflamed

[1]Institute for Bioinnovation, Biomedical Sciences Research Center "Alexander Fleming", Vari, Greece. [2]Institute for Fundamental Biomedical Research, Biomedical Sciences Research Center "Alexander Fleming", Vari, Greece. [3]Department of Physiology, Medical School, National and Kapodistrian University of Athens, Athens, Greece. [4]Present address: Institute for Research in Biomedicine (IRB Barcelona), Barcelona Institute of Science and Technology, Barcelona, Spain. [5]These authors contributed equally: Lida Iliopoulou, Christos Tzaferis, Alejandro Prados. e-mail: kollias@fleming.gr

intestine[10]. The results have facilitated the discovery of cell subsets that are enriched during the disease, the link between IBD-risk genes and specific cell clusters, the identification of crucial pathogenic pathways, and the correlation of gene signatures with treatment response[10].

On top of the well-studied hematopoietic cells and epithelial cells, intestinal fibroblasts have emerged as crucial regulators of intestinal inflammatory responses[9,11]. Different studies have highlighted the appearance of a pro-inflammatory type of fibroblasts during IBD, characterized by the expression of immune-related genes such as *Ccl19*, *Cd74*, and *Il11*[12–15]. However, the association of these IBD-related fibroblasts with the homeostatic subsets, as well as their spatial location in the intestine are poorly studied. Moreover, although, the cellular cross-talks between fibroblasts have been examined with more targeted in-silico approaches[12], their overall communication patterns during disease have not yet been fully appreciated.

In the present study, we utilize the $Tnf^{\Delta ARE}$ CD-ileitis mouse model to generate a single-cell atlas that describes the differentially activated signaling pathways, and the cellular interplays between the immune, and stroma cell compartments during ileitis. Through functional in vivo experiments involving manipulation of the *Tnfrsf1a* gene, we provide direct evidence for the critical role of distinct intestinal fibroblast subsets in organizing inflammation across different intestinal layers, thus contributing apart from the initiation to the chronicity of the disease. Additionally, we demonstrate that different fibroblast subsets are responsible for forming inflammation-associated structures in the lamina propria (tertiary lymphoid organs, TLO) and in the submucosa (granulomas). Thus, we pose spatially and functionally distinct fibroblast subsets as the exclusive TNF responder cells that orchestrate inflammation in the different intestinal locations, each driving the development of different histopathological features.

Results

Intestinal immune and stromal cell atlas of murine TNF-dependent ileitis

To address the cellular complexity of murine TNF-dependent ileitis, we analyzed the immune and stromal cells (in total 40,967 cells after filtering and doublet removal) isolated from the last 6 cm of the ileum from 3-month-old $Tnf^{\Delta ARE}$ ($n = 2$, total 18778 cells) and $Tnf^{+/+}$ ($n = 2$, total 22,189 cells) mice with established inflammation in lamina propria expanded in the submucosa and muscularis propria (SFig. 1a). We deliberately excluded epithelial cells from our analysis, as our primary focus was directed towards deciphering the cellular interactions between immune cells and stromal cells within the mucosal environment. To ensure sufficient representation of all the basic cellular compartments, especially given that stromal cells in $Tnf^{\Delta ARE}$ accounted for less than 10% of the total cell population, we sorted myeloid cells ($CD45^+CD11B/CD11C^+$), lymphoid cells ($CD45^+CD11B^-CD11C^-$), and stroma cells ($CD45^-EPCAM1^-$), mixed them to an equal ratio and performed scRNA-seq. (Fig. 1a, SFig. 1b). Initial analysis of each genotype separately, enabled us to acquire cells from the three primary cellular categories, based on the markers by which they were sorted (Fig. 1b, SFig. 1c).

Initially, we isolated and integrated the lymphoid cells from $Tnf^{+/+}$ and $Tnf^{\Delta ARE}$ mice and further subsetted them into 14 main clusters including B-cells, plasma cells, innate lymphoid cells (ILC), T cell subsets, natural killer T (NKT) cells and cycling lymphocytes (Fig. 1c, SFig. 2a, Supplementary Data 1). Among the lymphoid cells, we observed a dramatic increase in the relative abundance of B cells (Fig. 1d, SFig. 2b) in the $Tnf^{\Delta ARE}$ ileum. This increase was further validated through the analysis of the B/T cell ratio, which affirmed the substantial overabundance of B cells in comparison to other lymphocyte populations (Fig. 1e). Indeed, immunohistochemical analysis highlighted the expansion of B cells, distinctly segregated in lymphoid-like structures, the TLOs (Fig. 1f), previously reported to increase in the $Tnf^{\Delta ARE}$ ileum[6,16]. Although there was a higher relative prevalence of B cells, it is important to highlight that the overall count of intestinal lymphocytes, including IgA^+ plasma cells, was raised in $Tnf^{\Delta ARE}$ mice (SFig. 2c, d), indicating a more extensive immune cell infiltration within the intestine. This discrepancy underscores the need for cautious interpretation of relative abundance changes revealed by single-cell experiments, as they do not necessarily reflect alterations in absolute cell numbers. To detect transcriptional changes between the different genotypes, we performed differential expression analysis in the lymphoid cell clusters of $Tnf^{\Delta ARE}$ mice compared to healthy controls (Supplementary Data 2). Although the abundance of B cells was largely affected it was notable that the gene expression of newly infiltrated B cells did not exhibit substantial changes (Fig. 1g). Conversely, T cells, particularly memory T cells and T helper 17 (Th17 cells), displayed the most significant number of differentially expressed genes (DEGs) (Fig. 1g). Focusing further on the upregulated genes on T cell subsets, we used the Metascape portal[17] to infer molecular pathways, gene ontology (GO) terms and associations between them, enriched in $Tnf^{\Delta ARE}$ cells compared to heathy controls (Supplementary Data 3). Prominent biological functions governing T cell activation, such as the regulation of immune effector processes, lymphocyte proliferation, leukocyte cell–cell adhesion, and cellular response to interferon-beta, were markedly enriched within T cell clusters (Fig. 1h), including memory, TCRγδ, CD8, and Th17 cells (Fig. 1i). To identify the similarities in the lymphoid cells between murine and human ileitis, we performed correlation analysis between the $Tnf^{\Delta ARE}$ and a CD lymphoid dataset[18]. B cells, Plasma cells and ILC3s presented a high degree of correlation between diseased organisms (Fig. 1j). The T cell populations displayed robust correlations with a mixed population of human diseased T cells, with particularly strong and specific the correlation observed between mouse $CD8^+$ T cells and human CD8 and $CD8^+$ $KLRG1^+$ cells, as well as between mouse NKT cells and human NK cells and IELs ID3/ENTPD1, in addition to the correlation between mouse and human T regulatory T cells (Tregs), and mouse and human naïve T cells (Fig. 1j). This alignment in gene expression patterns between lymphoid cells in murine and human CD ileum is indicative of a noteworthy degree of transcriptional similarity during disease.

Collectively, these observations propose the expansion of B cells over the rest of lymphoid cells in the $Tnf^{\Delta ARE}$ ileum clustering in the emerging TLOs, and the transcriptional remodeling of T cell subsets towards acquiring more effector and memory functions.

A monocyte to $LYZ1^+$ macrophage lineage dominates the $Tnf^{\Delta ARE}$ ileum

We next sought to examine the heterogeneity of myeloid cells that infiltrate the inflamed murine ileum. After clustering them, we annotated 9 distinct subsets (SFig. 3a, Supplementary Data 1); including granulocytes, monocytes, 3 types of macrophages: resident, activated, (Resident & Activated Mfs), and macrophages with an intermediate phenotype between monocytes and mature macrophages (Intermediate Mfs), 4 clusters of dendritic cells (DC): conventional type 1 DC (cDC1), conventional type 2 DC (cDC2a and cDC2b) and plasmacytoid dendritic cells (pDC) (Fig. 2a, b). While in healthy mice, we barely detected granulocytes, they got massively increased in inflamed state, together with monocytes, activated macrophages and the cDC2b subset of DCs (Fig.2c, SFig. 3b)).

By mapping the expression of basic pro-inflammatory cytokines and chemokines in the myeloid clusters, we identified granulocytes and activated macrophages as the main cellular sources of distinct immune-related signals (Fig. 2d); Granulocytes highly express *Ccl3*, *Ccl4*, *Cxcl12* and important effector cytokines such as *Tnf* and members of the interleukin-1 (IL-1) family (*Il1a, Il1b, Il1rn*), while activated macrophages predominantly expressed *Ccl5*, *Cxcl1*, and members of the interleukin 6 (IL-6) family (*Osm*, *Il6*, and *Lif)*. In addition to these pro-inflammatory genes, activated macrophages were characterized by a

https://doi.org/10.1038/s41467-025-57570-7

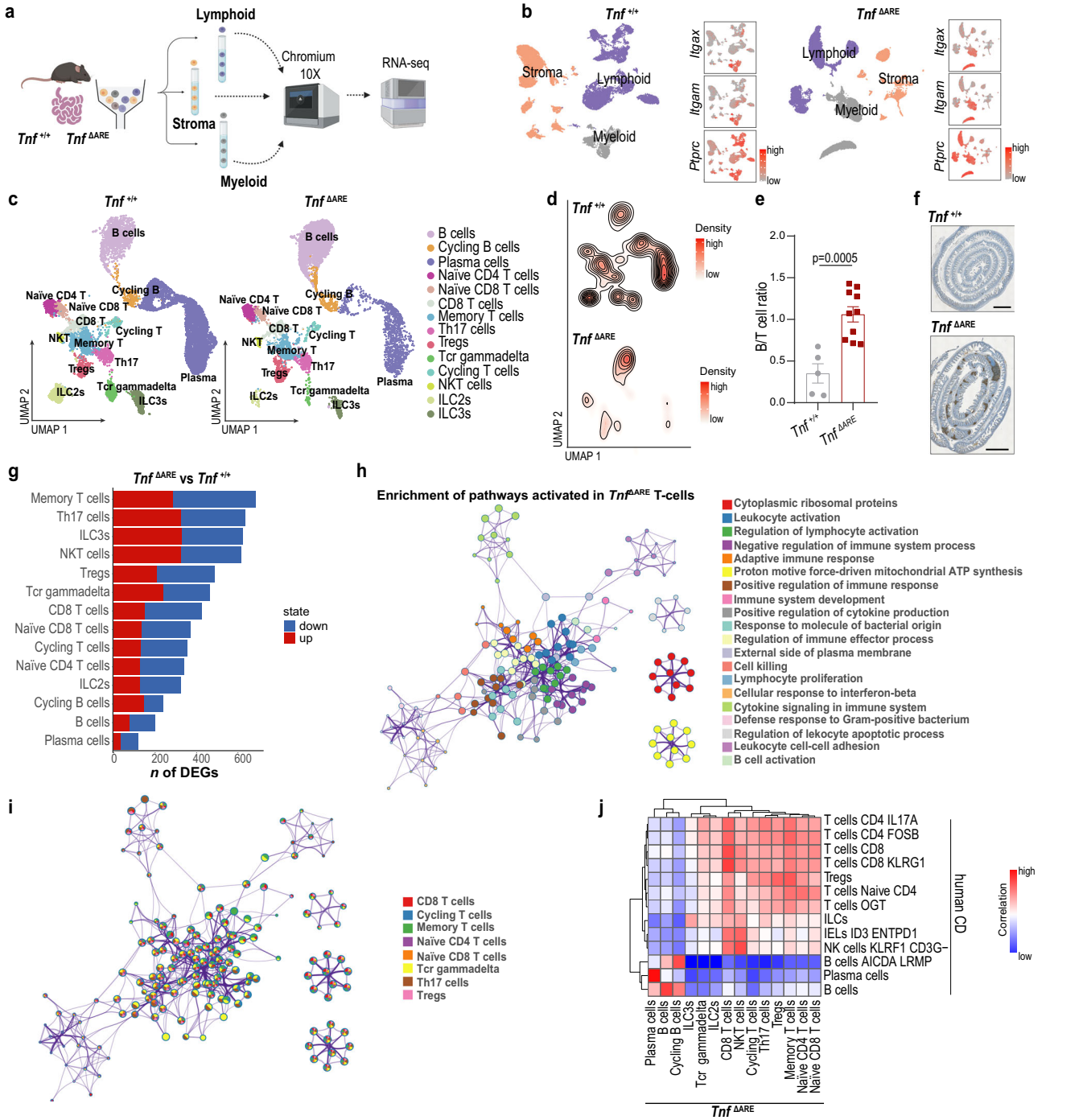

Fig. 1 | Lymphoid cell atlas of the *Tnf*$^{\Delta ARE}$ ileum. a Schematic representation of the experimental workflow. Created in BioRender. Kollias, G. (2025) https://BioRender.com/t35g730. **b** High-quality filtered ileal cells from *Tnf*$^{+/+}$ and *Tnf*$^{\Delta ARE}$ mice (3-month old) projected in UMAP space and colored by cell identity as stroma, lymphoid and myeloid cells. Normalized expression of *Itgam, Itgax and Ptprc* is depicted in feature plots (on the right side of umap plots). **c** UMAP projection of integrated *Tnf*$^{+/+}$ and *Tnf*$^{\Delta ARE}$ lymphoid cells. Cells are colored according to cluster assignment. **d** Contour plot showcasing cell density in the *Tnf*$^{+/+}$ and *Tnf*$^{\Delta ARE}$ UMAPs. **e** Ileal B to T cell number ratio in the ileum of 3-month old *Tnf*$^{+/+}$ and *Tnf*$^{\Delta ARE}$ mice quantified by flow cytometry, ($n = 5\&10$ mice/genotype), two-tailed unpaired Student's *t* test (Shapiro–Wilk normality test was used). Data are presented as mean values ± SEM. **f** Immunohistochemistry of B220^{+} cells in ileal swiss rolls from 3-month old *Tnf*$^{+/+}$ and *Tnf*$^{\Delta ARE}$ mice, scale bars=1 mm. **g** Barplots representing the number (n) of DEGs (two-tailed unpaired Wilcoxon rank sum test, $P_{val} < 0.01$ & average log(Fold Change) > 0.25) resulted from the comparison between *Tnf*$^{\Delta ARE}$ and *Tnf*$^{+/+}$ conditions in all lymphoid clusters. **h** Functional enrichment analysis (one-tailed hypergeometric test, $P < 0.01$, gene count > 2, and enrichment factor > 1.5) was performed on the upregulated genes in T cells (from **g**). Enriched terms were grouped into 20 categories, based on gene membership similarity, by Metascape. The network represents the clustering results, with terms colored according to their assigned categories. **i** Similar to (**h**), but the nodes in the network are displayed as pie charts, where the colors indicate the enrichment of each term across the upregulated genes of different T cell populations. In both (**h**) and (**i**), the size of each node corresponds to the gene count. **j** Correlation heatmap for lymphoid clusters in integrated data from *Tnf*$^{\Delta ARE}$ mice and CD patients. Spearman correlation was calculated using the average normalized expression values of the most highly variable genes. Source data are provided as a Source Data file.

https://doi.org/10.1038/s41467-025-57570-7

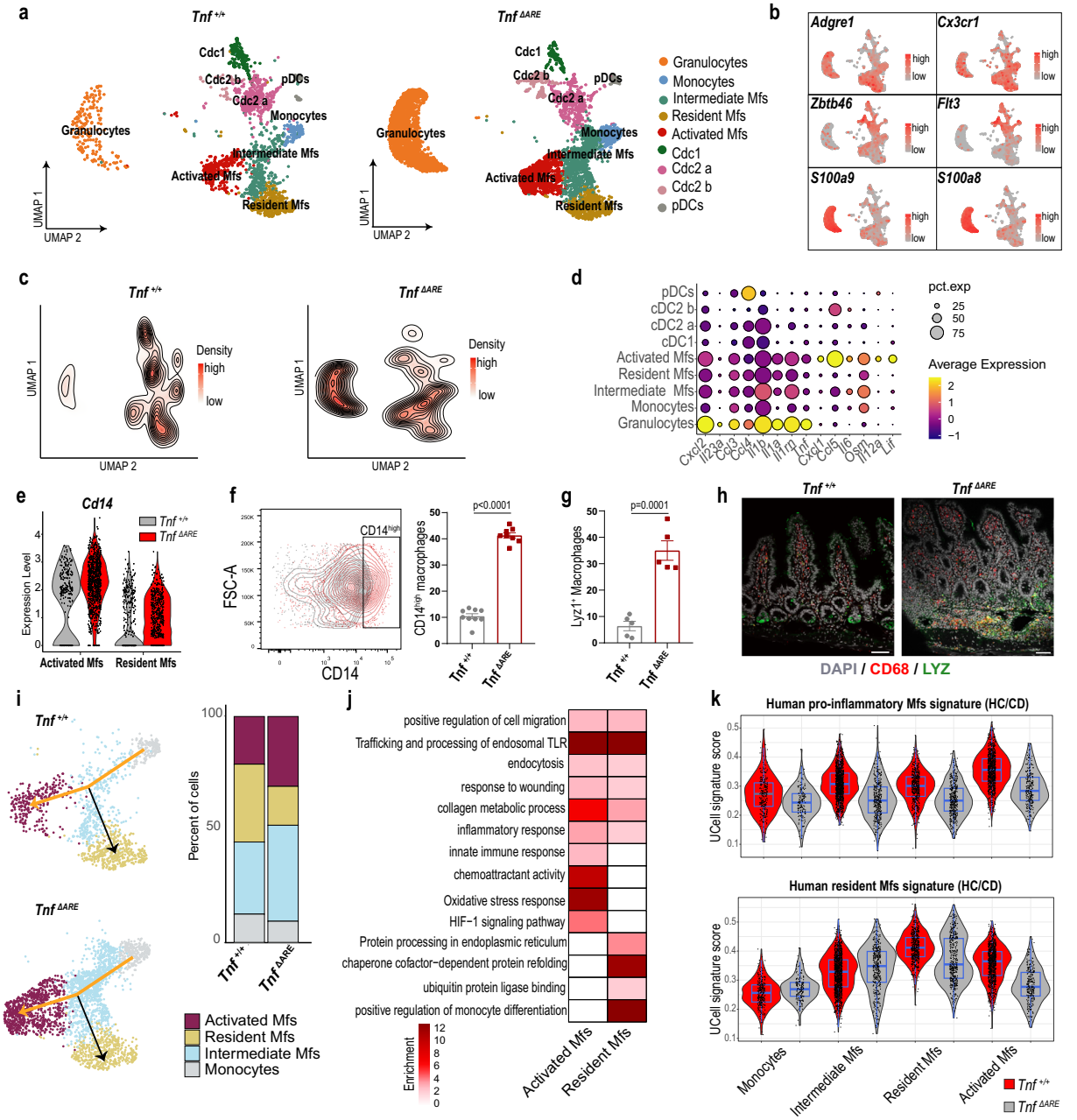

Fig. 2 | Transcriptome heterogeneity of ileal myeloid cells during inflammation. a UMAP embeddings plot, depicting subclusters of myeloid cells ($CD45^+CD11B^+CD11c^+$) from the ileum of 3-month-old $Tnf^{+/+}$ and $Tnf^{\Delta ARE}$ mice. **b** Feature plots displaying the normalized expression of gene markers associated with basic myeloid populations. **c** Contour plots depicting differences in the myeloid cell abundances between genotypes. **d** Dot plot showing z-scores of the average normalized gene expression of pro-inflammatory cytokines and chemokines per cluster. **e** Violin plots depicting normalized expression values of *Cd14* in Resident Macrophages and Activated Macrophages, ($Tnf^{+/+}$ in gray & $Tnf^{\Delta ARE}$ in red). **f** Representative gating strategy and quantification of $CD14^{high}$ macrophages ($n = 8\&9$ 3-month-old mice/genotype), two-tailed unpaired Student's t-test (Shapiro-Wilk normality test was used). **g** Quantification data of double $CD68^+LYZ1^+$ macrophages detected by immunofluoresence in cytospin preparations of ileal single cell suspensions from 3-month old $Tnf^{+/+}$ and $Tnf^{\Delta ARE}$, ($n = 5$ mice/genotype), two-tailed unpaired Student's *t* test (Shapiro–Wilk normality test was used). **h** Immunofluoresence staining of CD68 and LYZ1 in cryosections from the ileum of 3-month old $Tnf^{+/+}$ and $Tnf^{\Delta ARE}$ mice (scale bars = 50 μm). **i** Trajectory analysis depicting the two distinct lineages of myeloid cells color coded according to the final state and barplots representing the different cell subsets of the trajectory across genotypes. **j** Heatmap representing shared and unique pathways enriched in resident and activated macrophages identified using functional enrichment analysis (one tailed unpaired hypergeometric test, $P < 0.01$, gene count > 2, and enrichment factor > 1.5). **k** Violin plots showing gene-set signature scores of the CD-related human resident and pro-inflammatory macrophages gene signatures in the mouse myeloid clusters. Summary Statistics of boxplot metrics are presented in Supplementary Data 8. Data are presented as mean values ± SEM. Source data are provided as a Source Data file.

unique set of markers, including *Lyz1, Gpnmb*, and *Saa3* (SFig. 3a), along with high expression of *Cd14*, which distinguished them from resident macrophages that showed low *Cd14* expression (Fig. 2e). Flow cytometry confirmed the increase in the percentage of $CD14^{high}$ macrophages (Fig. 2f, SFig. 3c). Furthermore, *Lyz1*, a specific marker for Paneth cells[19], also showed increased expression in macrophages within the inflamed ileum of $Tnf^{\Delta ARE}$ mice (Fig. 2g, SFig. 3d). Notably, granulomas in the submucosa of $Tnf^{\Delta ARE}$ mice contained $LYZ1^+$

macrophages, indicating their preferential localization within these structures (Fig. 2h).

Trajectory analysis of macrophage populations using the Slingshot R package[20], uncovered the existence of two monocyte-derived lineages that share as a transitional point the intermediate macrophages and are characterized by two distinct final differentiation states, the resident and the activated macrophages (Fig. 2i). The lineage that leads to the resident macrophages was enriched in $Tnf^{+/+}$ mice while the activated macrophage lineage was over-represented in the $Tnf^{\Delta ARE}$ ileum (Fig. 2i, SFig. 3e), supporting the notion that monocyte-derived, inflammation-associated macrophages are originally separated from the resident intestinal macrophages.

In line with this, applying functional enrichment analysis with Metascape in the markers genes of resident and activated macrophages, highlighted distinc tmolecular pathways (Supplementary Data 3). Resident macrophages were characterized by pathways related to antigen presentation, whereas activated macrophages showed a dominant pro-inflammatory response, accompanied by oxidative stress (reactive oxygen species, ROS production), hypoxia, and collagen metabolism (Fig. 2j). Indeed, activated macrophages presented high expression of genes related to extracellular matrix (ECM) degradation (*Mmp9, Mmp12, and Mmp14*) (SFig. 3f) previously associated with the granuloma-related macrophages[21]. Although activated and resident macrophages display only a few differentially expressed genes during disease progression (SFig. 4a, Supplementary Data 2) relative to other myeloid cells, an unbiased single sample gene set enrichment analysis (ssGSEA) across all populations confirmed the significant enrichment of pathways associated with ECM and collagen degradation, as well as hypoxic responses, specifically in the $Tnf^{\Delta ARE}$ activated macrophage population (SFig. 4b. Supplementary Data 4).

Previous scRNA-seq analysis in the ileum of human CD patients stressed the existence of two macrophage subsets, attributed as resident and pro-inflammatory macrophages[12]. Calculating gene signature scores, utilizing their top marker genes (Supplementary Data 5), in mouse myeloid cells suggested a strong association of human and mouse resident macrophages and a substantial correspondence of human CD pro-inflammatory macrophages with the activated and intermediate $Tnf^{\Delta ARE}$ macrophage subsets (Fig. 2k).

These findings highlight the robust infiltration and inflammatory activation of myelod subpopulations in the inflamed ileum, particularly within granuloma regions, as well as shared transcriptional profiles of disease-associated ileal macrophages in human and murine CD-ileitis.

Compositional and transcriptional remodeling of stroma cells during ileitis

Following the analysis of immune cells, we aimed to characterize in detail the stromal cells during intestinal inflammation. Integration and unsupervised clustering revealed 14 cellular clusters (Supplementary Data 1). Detailed examination of representative markers identified clusters of endothelial cells, (EC),(lymphatic, vein, and capillary), fibroblasts (telocytes, trophocytes, Pdgfra^{lo}Cd81^{-}, fibroblastic reticular cells or FRCs, Follicular dendritic cells/Marginal reticular cells or FDC/MRC), smooth muscle cells (SMC), glial cells, mesothelial cells, interstitial cells of Cajal and pericytes (Fig. 3a, SFig. 5a, b)[9]. We next assessed the relative abundance of stromal cell clusters in $Tnf^{+/+}$ and $Tnf^{\Delta ARE}$ mice. We detected a marked reduction in fibroblast subsets (telocytes, trophocytes, Pdgfra^{lo}Cd81^{-}) and a relative expansion of lymphatic endothelial cells (LEC) and FRC populations (FRC1&FRC2) (Fig. 3b, SFig. 5c). The overrepresentation of FRCs was expected in the areas where TLOs developed[16,22]. Indeed, we validated the decline in the overall population of fibroblasts, both as number and percentage in 3-month-old $Tnf^{\Delta ARE}$ mice (Fig. 3c, SFig. 5d), suggesting that the composition of stromal cells is affected, possibly due to the shortening and blunting of the inflamed villi in the ileal mucosa. Following the dominant changes in their relative abundance, fibroblast subsets exhibited the highest number of DEGs (telocytes: 998, Pdgfra^{lo}Cd81^{-}: 809, trophocytes: 669) together with LECs (781) and SMCs (823) (Fig. 3d, Supplementary Data 2). In contrast, FRCs showed minimal gene expression alteration compared to wild-type subsets (FRC1: 158, FRC2: 152) (Fig. 3d). Enrichment analysis in the upregulated genes of stromal subsets during disease, highlighted a strong pro-inflammatory signature acquired primarily by the telocytes, trophocytes, Pdgfra^{lo}Cd81^{-}, capillary ECs, and SMCs (Fig. 3e, Supplementary Data 3). This was characterized by pathways associated with cytokine response (TNF signaling pathway, response to interleukin-1, response to type II interferon), innate immune response (NOD-like receptor signaling pathway, response to lipopolysaccharide, regulation of chemotaxis), and antigen presentation (antigen processing and presentation). Fibroblast together with endothelial cell clusters upregulated also genes related to vasculogenesis and new blood vessel cell formation (Fig. 3e). Implementation of impartial ssGSEA including all expressed genes, validated the robust proinflammatory activation of fibroblast subsets, SMCs and Vein ECs (SFig. 5e, Supplementary Data 4). Although chronic $Tnf^{\Delta ARE}$ ileitis in mice has recently been associated with the development of intestinal fibrosis[23]—a topic of some debate[24]—Sirius Red staining on mice at both 3 and 6 months of age, did not reveal collagen deposition in neither early nor chronic ileitis stages (SFig. 5f). These findings aligned with the observed reduction or lack of change in the expression of various ECM genes, including collagens and *Fn1* (SFig. 5g), as well as decreased activity in the pro-fibrotic transforming growth factor beta (TGFβ) pathway within $Tnf^{\Delta ARE}$ fibroblast subsets (SFig. 5h). To examine the relevance of our data with human CD, we performed correlation analysis with a previously reported stromal cell dataset including cells from CD inflamed ileum, uninvolved areas, and healthy specimens[18]. There was a strong and specific correlation between mouse and human diseased endothelial subtypes, glial cells, pericytes, and myofibroblasts/SMCs (Fig. 3f). Regarding fibroblast subtypes, human CD fibroblasts SFRP2 SLPI and KCNN3 LY6H were mostly correlated with $Tnf^{\Delta ARE}$ trophocytes, while CD fibroblasts NPY SLITRK6 were best correlated with $Tnf^{\Delta ARE}$ telocytes (Fig. 3f). Among fibroblasts, the ADAMDEC1, the activated ADAMDEC1 CCL19 and the SMOC2 PTGIS clusters were equally similar to all mouse fibroblast subsets, suggesting that these human clusters represent a mixed population of cells corresponding to mouse subsets (Fig. 3f). Notably, the broad correlation of the activated ADAMDEC1 CCL19 fibroblasts with the $Tnf^{\Delta ARE}$ subsets proposes that CD-associated cell subsets (like the CCL19^{+} fibroblasts) may be reflected in various mouse fibroblasts populations and may not represent nessecerily unique disease emerging clusters.

To further assess the relevance of the $Tnf^{\Delta ARE}$ model, we conducted a re-analysis of fibroblast scRNA-seq data from Dextran Sulfate Sodium (DSS)—induced colitis[25] and integrated these findings with our own fibroblast subsets. This comparative analysis demonstrated a high degree of concordance among populations (SFig. 6a): the Pdgfra^{lo}Cd81^{-} subset aligned closely with the S1 subset, trophocytes with S3 cells, and telocytes with the S2 subset. Notably, the pro-inflammatory S4 subset clustered with the FRC1 population, suggesting that S4 may correspond to pre-existing FRC subsets rather than representing a novel fibroblast state. Focusing on the three fibroblast populations (telocytes, Pdgfra^{lo}Cd81^{-} and trophocytes) and their corresponding subsets within the DSS dataset, differential expression analysis revealed both a core set of commonly deregulated genes during inflammation and a larger group of genes uniquely up- or downregulated in each disease model (SFig. 6b). Metascape analysis of the upregulated genes highlighted a shared set of enriched pathways across both models, including inflammatory response, TNF and IFNβ signaling, cell chemotaxis, and endothelial cell proliferation (SFig. 6c). However, distinct pathways were enriched specifically in fibroblasts from each disease. DSS fibroblasts displayed enhanced pathways

https://doi.org/10.1038/s41467-025-57570-7

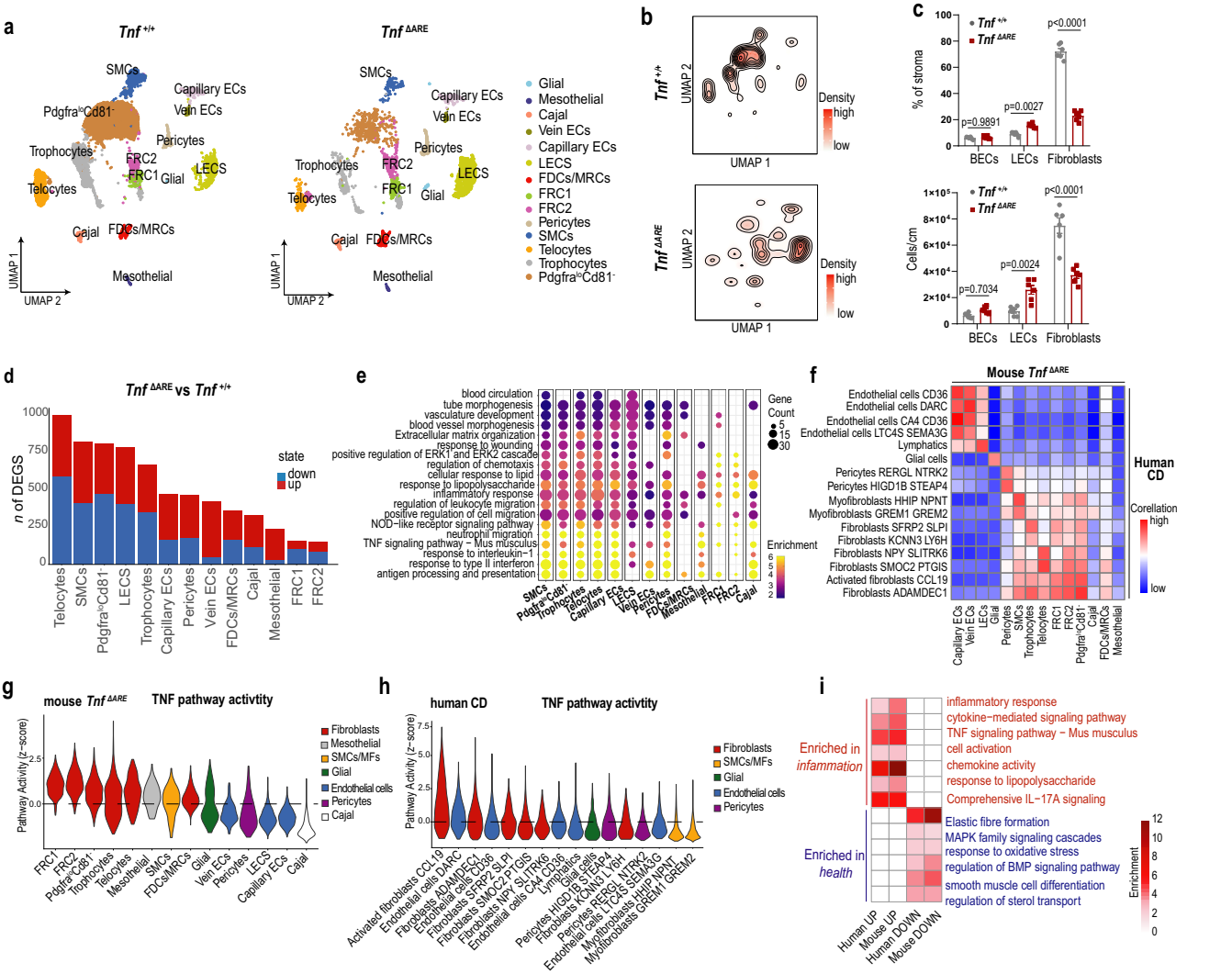

Fig. 3 | Fibroblast compositional and transcriptional alterations upon inflammation in the ileum. a UMAP representation of ileal stromal cells (CD45$^-$EPCAM$^-$) in 3-month old *Tnf*$^{+/+}$ and *Tnf*$^{\Delta ARE}$ mice. **b** Contour plot overlaid on UMAP projections depicting the cell abundances of stromal cell subsets. **c** Flow cytometry analysis of the absolute number and percentage (in the CD45$^-$EPCAM$^-$ cells) of endothelial cells and fibroblasts in the ileum of 3-month-old mice with the indicated genotypes. Each dot represents sample from one mouse, ($n = 6$ mice/genotype), Normality was assessed by the Shapiro–Wilk test, 2-way Anova with Sidak's correction was used. Data are presented as mean values ± SEM. **d** Barplots showing the number of DEGs in the stromal clusters (*Tnf*$^{\Delta ARE}$ versus *Tnf*$^{+/+}$, two-tailed unpaired Wilcoxon rank sum test, Pval <0.01 & average log(Fold Change) > 0.25). **e** Dotplot depicting enriched functional terms in the upregulated genes of *Tnf*$^{\Delta ARE}$ clusters.Terms were identified using one-tailed unpaired hypergeometric test ($P < 0.01$, gene count > 2, enrichment factor > 1.5). Dot color represents the enrichment factor, while dot size indicates the gene count. **f** Correlation heatmap for stromal populations in integrated data from *Tnf*$^{\Delta ARE}$ mice and CD patients. Spearman correlation was calculated using the average normalized expression values of the most highly variable genes. **g**, **h** Violin plots showing z-scores of TNF pathway activity in *Tnf*$^{\Delta ARE}$ (**g**) and human CD (**h**) stromal cells. Cells are grouped according to their cluster annotation and are colored by superclusters. Myofibroblasts (MFs) **i** Heatmap displaying shared overrepresented and underrepresented functional terms of mouse and human diseased fibroblast superclusters. Source data are provided as a Source Data file.

related to ECM interaction, collagen biosynthesis, and wound response, likely reflecting the acute mucosal barrier disruption and subsequent resolution of inflammation. In contrast, *Tnf*$^{\Delta ARE}$ fibroblasts exhibited strong signatures in antigen presentation, leukocyte activation, and regulation of neuronal projection, underscoring differences in immune and cellular responses between acute and chronic models. Since TNF is the driver pathway for the development of ileitis, we inferred the TNF pathway activity scores on the stromal cell subsets using *PROGENy*[26]. Surprisingly, *Tnf*$^{\Delta ARE}$ fibroblasts subsets (FRC1, FRC2, telocytes, Pdgfra^{lo}Cd81$^-$, and trophocytes) presented the highest activation of TNF pathway (Fig. 3g). Of note, the same analysis on immune populations underscored the high activation of TNF pathway in granulocytes, monocytes and macrophage clusters (SFig 6d). Interestingly, human CD fibroblasts and especially the disease-associated ADAMDEC1 CCL19 cluster, were also having an enriched TNF pathway activity together with two subtypes of endothelial cells (Fig. 3h). Organization of the identified cell subsets in superclustersin human and mouse datasets (Supplementary Data 6) and subsequent differential gene expression and pathway enrichment analysis in CD versus healthy fibroblasts in both mouse and human unveiled common pathways over-or under-represented in disease (Fig. 3i). Among the shared enriched biological processes, all related to immune-mediated functions, we stress the upregulation of response to TNF which was evident in both human and mouse diseased fibroblasts as opposed to healthy fibroblast clusters (Fig. 3i).

Overall, our analysis in stromal cell subsets reveal that despite the reduced number of fibroblasts subsets during ileal inflammation, their activation is significantly skewed towards a pro-inflammatory

https://doi.org/10.1038/s41467-025-57570-7

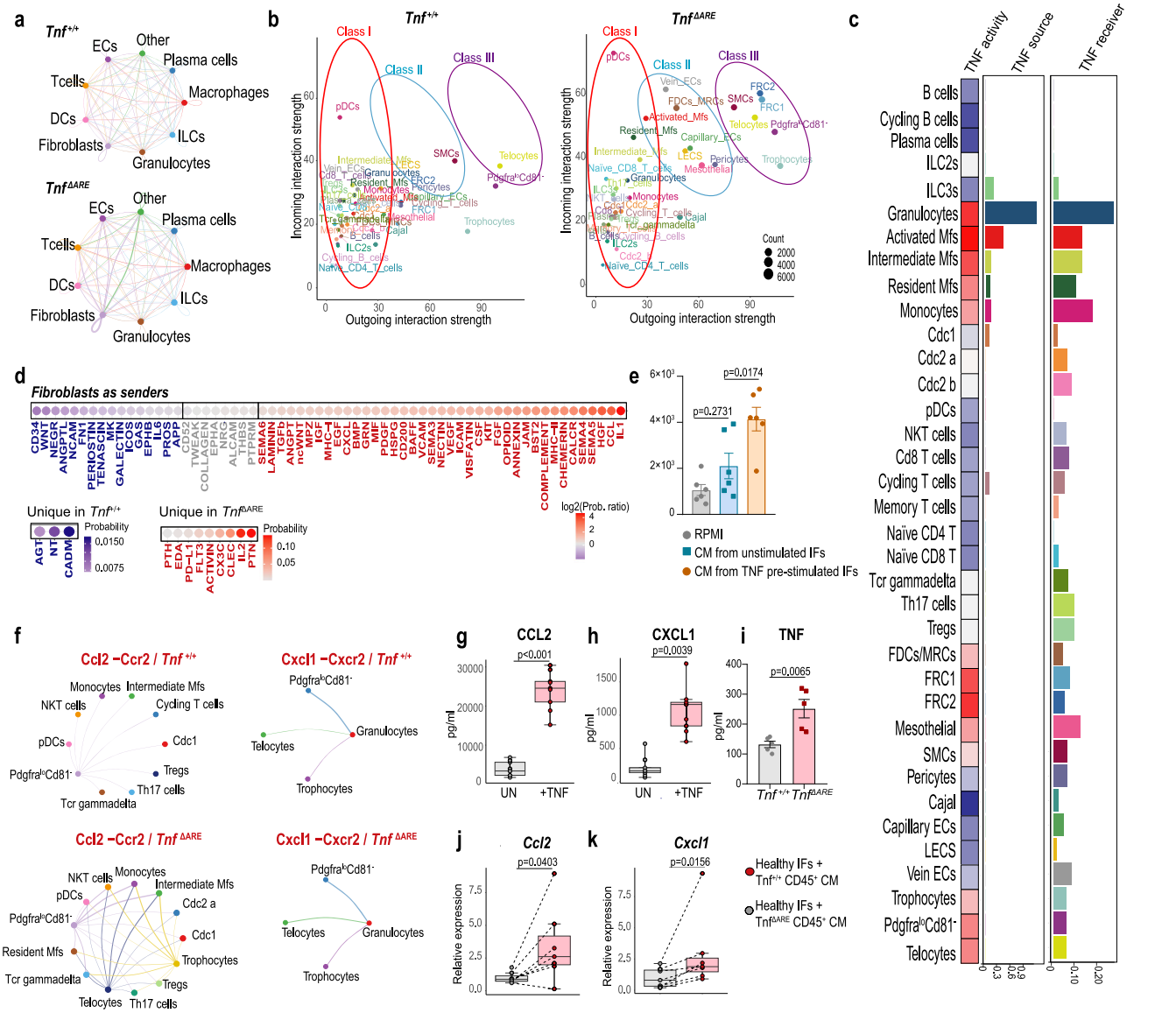

Fig. 4 | Cell–cell communication analysis reveals active signaling pathways in ileal homeostasis and inflammation. a Cell-to-cell communication networks between cell subsets in *Tnf*$^{+/+}$ and *Tnf*$^{\Delta ARE}$ conditions. Edge width represents communication strength between cell groups. **b** Scatter plots showcasing the differences in incoming and outgoing interactions of each cluster between conditions. **c** Heatmap and bar plots for TNF pathway activity scores per cluster and aggregated CellChat communication probability. **d** Dotplots of shared and sample specific signaling pathways with fibroblasts as senders cells. The top dot plot shows the log2 ratio of communication probabilities (log2Prob.ratio), while the two bottom dot plots display the communication probability per sample. **e** Quantification of live migrating myeloid (CD11B^{+}) cells plated in a transwell system and assessed after 16 h. Ordinary one-way Anova with Tukey's correction. ($n = 6$ mice/condition) **f** Signaling networks for the interactions of Ccl2-Ccr2 (top two plots) and Cxcl1-Cxcr2 (bottom two plots) in *Tnf*$^{+/+}$ and *Tnf*$^{\Delta ARE}$ conditions. The presence of an edge connecting clusters indicates active interactions, while edge width represents interaction strength. **g**, **h** Quantification of CCL2 and CXCL1 by Elisa in primary ileal fibroblasts stimulated with TNF (10 ng/ml); ($n = 9$ biological samples/condition), two-tailed paired Student's *t* test (**g**) and two-tailed Wilcoxon test (**h**). **i** Quantification of TNF by Elisa in isolated CD45^{+} cells, cultured for 24 h. ($n = 7$ mice/genotype), two-tailed unpaired Student's *t* test. Data are presented as mean values ± SEM. **j**, **k** *Ccl2* and *Cxcl1* quantification by qPCR in cultured primary ileal fibroblasts (IFs) stimulated with conditioned media (CM) from intestinal CD45^{+} cells, isolated from *Tnf*$^{+/+}$ and *Tnf*$^{\Delta ARE}$ mice and cultured for 24 h; ($n = 7$ biological samples/condition), two-tailed paired Student's *t* test (**j**) and two-tailed Wilcoxon test (**k**) Normality was assessed by the Shapiro–Wilk test. Cells from 3-month-old mice were used in (**e**, **i**) and from 2–4-month-old mice in (**j**, **k**). Boxplot summary statistics for (**g**–**k**) are presented in Supplementary Data 8. Source data are provided as a Source Data file.

phenotype. Importantly, all fibroblast subsets acquire similar properties, implying that each of them plays a substantial role in the development of the disease. In addition, this activation pattern shares striking resemblances with human CD subtypes, notably featuring pronounced TNF pathway activation.

Fibroblast communication patterns in the *Tnf*$^{\Delta ARE}$ ileum

To infer the cellular connectome in the diseased and healthy ileum, we performed comparative cell-to-cell communication analysis using *CellChat*[27]. To generate a more simplified communication network, we categorized the cells into superclusters and visualized the number of interaction signals (Fig. 4a, SFig. 7a). Surprisingly, among the most evident changes in the *Tnf*$^{\Delta ARE}$ mice was the enhanced paracrine and autocrine fibroblast signals (Fig. 4a). Comparing the strength of outgoing and incoming interactions in a two-dimensional space, facilitated the identification of three cellular hubs that display noteworthy variations in their ability to send or receive signals (Fig. 4b). Class I includes cell subsets characterized by relatively low levels of both

incoming and outgoing signals, with the exception of pDCs. Class II incorporates cells demonstrating moderate strength in receiving and sending signals, while Class III encompasses cell clusters displaying high signal transmission and medium receiving capacity. Significantly, in the *Tnf*$^{\Delta ARE}$ mice, all fibroblast subsets and SMCs were prominently represented within the Class III hub, indicating their role as quantitatively primary cellular sources of signals. Conversely, in contrast to healthy mice, the Class II hub in *Tnf*$^{\Delta ARE}$ mice comprised endothelial cell types, pericytes, mesothelial cells, and activated macrophages, all exhibiting relatively balanced incoming and outgoing capacities (Fig. 4b).

Next, we visualized the differential number of interactions between the two datasets, including all the cell cluster pairs (SFig. 7b). Interestingly, notable modifications were observed in the paracrine and autocrine signaling patterns specifically within the FRC and FDCs/MRC populations (SFig. 8, SFig. 9). These subsets of fibroblasts primarily reside in the Peyer's Patches (PP) and TLOs, where they play a crucial role in supporting the structural integrity and functionality of these lymphoid structures[28]. To further investigate the necessity of PPs and TLOs in the progression of ileitis, we impeded their formation in *Tnf*$^{\Delta ARE}$ mice by deleting the *Ltbr* gene, which is crucial for the development of peripheral lymphoid organs. As a result, *Ltbr*^{KO} *Tnf*$^{\Delta ARE}$ mice completely lacked PPs and TLOs (SFig. 10a). However, the severity of ileitis remained unaffected by the absence of these lymphoid organs in the ileum, indicating that they are dispensable for the initiation and progression of intestinal inflammation (SFig. 10b). This implies that although FRCs/FDCs/MRCs exhibit an increased number of outgoing and incoming signals, which may be important for the formation of ectopic TLOs in the ileum of *Tnf*$^{\Delta ARE}$ mice, they are not actively involved in the propagation of inflammation.

Thus, we focused on the communication pattern of non-FRC fibroblasts (trophocytes, telocytes, Pdgfra^{lo}Cd81^{-}) that exhibited an increased ability to transmit and receive signals during ileitis. The calculation of communication probabilities relies on the evaluation of ligand and receptor expression within cells belonging to particular clusters[26]. Focusing on TNF pathway, we observed no significant upregulation of *Tnfrsf1a (Tnfr1)*, and a modest increase in *Tnfrsf1b* (*Tnfr2)* expression during ileitis (SFig. 7c). However, there was clear evidence of TNF overexpression in granulocytes, activated macrophages, and to a lesser extent, in other myeloid cells (Fig. 4c, SFig. 7c). In addition, applying the *PROGENy* algorithm in all *Tnf*$^{\Delta ARE}$ subsets revealed the activation of TNF pathway (incorporating molecular mediators and downstream target genes) primarily in myeloid cells and secondary to fibroblast subpopulations (including telocytes, trophocytes and Pdgfra^{lo}Cd81^{-}) (Fig. 4c).

By calculating the differential aggregated probability score between diseased and healthy mice, we observed signals originating from (Fig. 4d) or targeting (SFig. 7d) fibroblasts that were enriched in either *Tnf*$^{\Delta ARE}$ or wild-type mice (Supplementary Data 7). Examples of eliminated fibroblast-derived signals during ileitis include the expression of CD34 and WNT ligands, related among other to epithelial cell homeostasis and NCAM ligands that are related to neuronal functions (Fig. 4d). On the other hand, in the upregulated ligands, there was an augmented expression of chemotactic molecules (such as CCLs, CXCLs, SEMA3/4/5/6, and CHEMERIN), adhesion mediators (like ICAM), and pro-inflammatory activators of immune effector cells (including COMPLEMENT, IL1, IL2, FLT3, BAFF, and MHCI/II) (Fig. 4d). Among the fibroblast-targeting signaling pathways, we observed an upregulation of ECM interactions (COLLAGEN, LAMININ) and pro-inflammatory cytokines, including IL-1, type II interferons and STAT3 activators (IL6, OSM, LIFR) (SFig. 7d), all of them reported to be implicated in anti-TNF non-response mechanisms[29–31].

Given that CCL and CXCL families were among the top upregulated signals originating from fibroblasts (Fig. 4d), we ex vivo validated that TNF-prestimulated fibroblasts, through their secretome, can enhance the migration capacity of myeloid cells (Fig. 4e). We then calculated the differential aggregated probability scores for specific ligand-receptor pairs within these categories (SFig. 11a). Notably, we observed a strong activation of the CCL2 and CXCL1 pathways, mediated through the receptors Ccr2, Ackr1, and Ackr2 for CCL2, and Cxcr2 and Ackr1 for CXCL1 (Fig. 4f, SFig. 11b). Our focus was on the Ccl2-Ccr2 and Cxcl1-Cxcr2 ligand-receptor pairs, as the target cells included diverse types of myeloid cells (SFig. 11c).

To determine whether TNF can directly induce the upregulation of Ccl2 and Cxcl1, we stimulated primary intestinal ileal fibroblasts with TNF, which resulted in a significant increase in the secretion of both CCL2 and CXCL1 (Fig. 4g, h). To further investigate this interaction in a system relevant to the *Tnf*$^{\Delta ARE}$ model, we cultured immune cells from the ileum of *Tnf*$^{\Delta ARE}$ mice, which exhibit elevated TNF production (Fig. 4h), alongside immune cells from healthy ileal tissue. We broadly included various immune cell types, as previous work from our lab has demonstrated that multiple sources of TNF (including epithelial cells, myeloid cells, and T cells) are sufficient for the development of *Tnf*$^{\Delta ARE}$ pathology[6,32]. When healthy ileal fibroblasts were stimulated with conditioned media from *Tnf*$^{\Delta ARE}$-derived immune cell cultures, we observed upregulation of both *Ccl2* and *Cxcl1* expression, compared to healthy immune cell cultures (Fig. 4i, j). This ex vivo system demonstrates that fibroblasts can be primed by the high-TNF-expressing *Tnf*$^{\Delta ARE}$ immune microenvironment to produce chemokines such as CCL2 and CXCL1.

Given the crucial role of fibroblasts during ileitis suggested by our bioinformatic analysis, we aimed to examine fibroblast alterations at a very early, pre-disease stage. We selected 3-week-old mice that were free from histologic signs of disease (SFig. 11d) and showed no immune cell infiltration in the ileum (SFig. 11e). Notably, fibroblasts at this stage were already activated, as indicated by the expression of the adhesion molecule Vascular cell adhesion protein 1 (VCAM-1) (SFig. 11f) and elevated levels of the chemoattractants *Ccl2* and *Cxcl1* (SFig. 11g, h).

In summary, among all cell types in the ileum (excluding epithelial cells), fibroblast subsets exhibit the highest propability of acting as sender cell types during the disease, driving inflammation through different chemotactic and immune-activating signals*, such as Ccl2 and Cxcl1* These molecules are already elevated before disease onset, underscoring the critical role of fibroblasts as coordinators of ileitis.

Differential targeting of spatially organized fibroblast subpopulations in the inflamed ileum

Due to the striking transcriptional activation of fibroblast subsets, we aimed to identify their spatial organization during the development of ileitis. We conducted disease evaluation on *Tnf*$^{\Delta ARE}$ mice at different stages of their development (Fig. 5a). At 3 weeks of age, histological assessment revealed an absence of inflammatory infiltrates. However, at 8 weeks, inflammation in the lamina propria had initiated, accompanied by mild infiltration in the submucosal layer. As the mice reached 3 and 6 months of age, the submucosal layer underwent massive enlargement, leading to an increased submucosal thickness. Notably, in this area, fibroblasts showed a specific expansion according to their spatial distribution. Additionally, the muscularis mucosa displayed mild infiltration at a later disease stage (3 months) and became more established by 6 months of age (Fig. 5a).

We next used two different fibroblast-specific cre lines to target intestinal fibroblasts; the *Twist2*^{cre} and the *Col6a1*^{cre} mice[33,34]. Crossing these mice with the *R26*^{mTmG} reporter strain[35] revealed that *Twist2*^{cre} efficiently targeted a significant proportion of fibroblasts (approximately 65%), while *Col6a1*^{cre} seemed to have a more restricted targeting efficiency (approximately 50%) (SFig. 12a–c). Both cre lines showed minimal targeting efficiency in CD45^{+} immune cells, neutrophils and macrophages (SFig 12a–c). Upon conducting a more detailed analysis, we found that the *Twist2*^{cre} line exhibited broad specificity across fibroblast subpopulations, including telocytes, trophocytes, and

https://doi.org/10.1038/s41467-025-57570-7

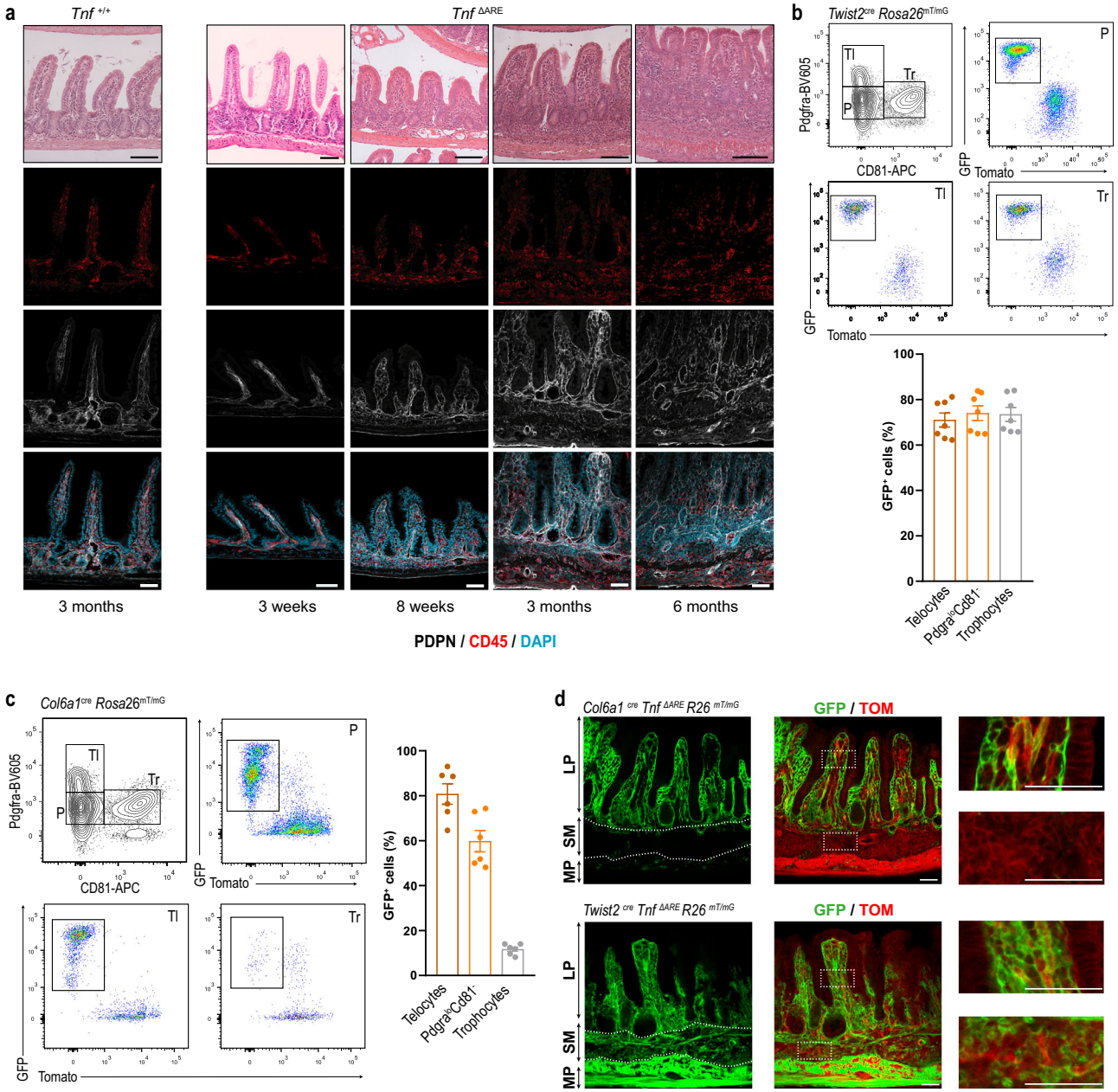

Fig. 5 | *Col6a1*^{cre} and *Twist2*^{cre} fibroblast-specific targeting in the ileum. a H&E images of 4-μm-thick ileal paraffin sections and immunofluorescent confocal images from 12-μm-thick ileal cryosections, stained with DAPI and antibodies against Podoplanin (PDPN) and CD45. Images are representative of 3 mice per condtition. **b**, **c** Flow cytometry analysis of Live/Lin$^-$/Pdpn$^+$ ileal fibroblasts from the ileum of 2–3-month-old Twist2^{cre} R26$^{mT/mG}$ ($n = 7$ mice/population) (**b**) and Col6a1^{cre} R26$^{mT/mG}$ ($n = 6$ mice/population) (**c**) reporter mice. Quantification of GFP$^+$Tom$^-$ populations is represented as a percentage in the different fibroblast subsets. Tl:Telocytes, P: Pdgfra^{lo}Cd81$^-$, Tr: Trophocytes. **d** Representative confocal images from the ileum of 3-month-old *Twist2*^{cre} *R26*$^{mT/mG}$ *Tnf*$^{\Delta ARE}$ and *Col6a1*^{cre} *R26*$^{mT/mG}$ *Tnf*$^{\Delta ARE}$ mice. White dashed boxes indicate areas of higher magnification depicted on the right. LP lamina propria, SM submucosa, MP muscularis propria. Scale bars = 50 μm. Data are presented as mean values ± SEM. Source data are provided as a Source Data file.

Pdgfra^{lo}Cd81$^-$ fibroblasts (Fig. 5b). In contrast, the *Col6a1*^{cre} mice, similarly to published results[36], displayed high specificity for telocytes (approximately 80%) and Pdgfra^{lo}Cd81$^-$ fibroblasts (approximately 60%), but their targeting efficiency for trophocytes was notably low (approximately 10%) (Fig. 5c). In addition, both Cre lines show similar target the majority of Podoplanin$^+$ FRCs inside the isolated lymphoid follicles (ILFs) (SFig. 12d).

Given this discrepancy in targeting homeostatic fibroblast subpopulations, we were intrigued to investigate whether these distinct patterns of targeting persisted in the *Tnf*$^{\Delta ARE}$ ileum. Since, telocytes are loosing the high expression of Pdgfra in the *Tnf*$^{\Delta ARE}$ mice (both in mRNA and protein level) (SFig. 12 e, f), we decided to investigate the specificity of fibroblast populations through immunofluorescence in the inflamed ileum. During an advanced disease stage (3 months), we found that *Twist2*^{cre} expressing cells were widely distributed throughout the inflammatory lesions, including areas where telocytes are typically found (subepithelial regions), intra-villus space, the submucosal layer, and even within the muscle layer (Fig. 5d). Interestingly, myocytes also expressed GFP, both in the circular and longitudinal muscle layers (Fig. 5d). On the other hand, fibroblasts targeted by the *Col6a1*^{cre} exhibited a different distribution pattern, being exclusively present in the lamina propria, including subepithelial regions, and inside the villus space Notably, the *Col6a1*^{cre} line did not target fibroblasts in the submucosal layer (Fig. 5d).

Taken together, these results indicate that the *Twist2*^{cre} strain shows broad specificity towards fibroblasts in both healthy and *Tnf*$^{\Delta ARE}$ ilea. However, the *Col6a1*^{cre} line, which specifically targets telocytes and Pdgfra^{lo}Cd81^{-} subsets in healthy mice, exhibits restricted targeting efficiency in the inflamed lamina propria of *Tnf*$^{\Delta ARE}$ mice.

Different fibroblast subsets are responsible for triggering and advancing ileal inflammation via TNFR1 signaling

Given the high activation of TNF signaling in *Tnf*$^{\Delta ARE}$ fibroblasts as revealed by our scRNA-seq analysis, we sought to identify the role of *Tnfrsf1a* (gene encoding the TNFR1, the major receptor for TNF) expressed in fibroblasts during ileitis progression.

To delve into this, we generated fibroblast-specific *Tnfrsf1a* deficient *Tnf*$^{\Delta ARE}$ mice using the *Col6a1*^{cre} line. Depletion of *Tnfrsf1a* in telocytes and Pdgfra^{lo}Cd81^{-} cells completely prevented the onset of ileal inflammation at 3 months of age (Fig. 6a), as well as the formation of submucosal granulomas and the numerical expansion of TLOs (SFig 13a, b) Even at the chronic disease stage (6 months), the mice only exhibited minimal immune cell infiltration, primarily confined to the submucosal layer (Fig. 3b, c). These findings underscore the critical

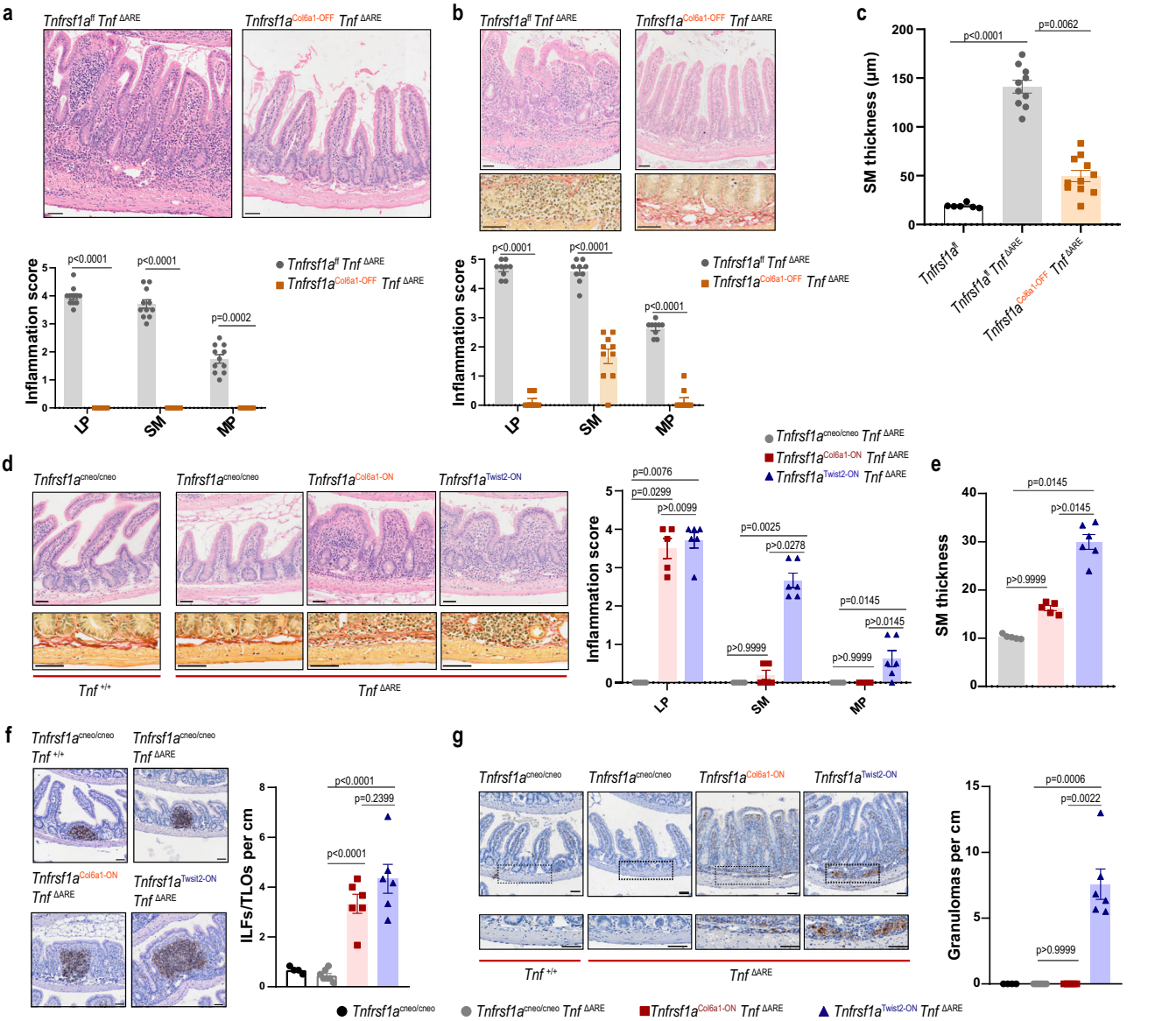

Fig. 6 | Distinct fibroblast populations orchestrate ileitis development and progression in the different intestinal layers. a, **b** Representative H&E stained histological images and inflammation scoring of the different intestinal layers in the ileum of 3-month (**a**) and 6-month (**b**) old mice with the indicated genotypes. Additionally, representative images of the ileal submucosal layer stained with Sirius Red in 6-month-old mice; (n = 6&11 mice/ genotype), two-tailed Mann–Whitney's test. Normality was assessed by the Kolmogorov–Smirnov test. **c** Quantification of the submucosal (SM) thickness (μm) in 6 month-old mice with the indicated genotypes; (n = 10 mice/genotype), Kruskal–Wallis test was used with Dunn's correction. **d**, **e** (**d**) Inflammation scoring in the different ileal layers and representative H&E and Sirius Red images of 4-month-old mice. **e** Submucosal thickness quantification; (n = 5&6 mice/ genotype), Kruskal–Wallis test was used with Dunn's correction (**d**) and one-way Anova with Tukey's correction was used. Normality was assessed by the Kolmogorov–Smirnov test. **f** Representative B220^{+} stainings and quantification of ILFs/TLOs in 4-month-old mice with the indicated genotypes; (n = 4,6,7 mice/genotype), one-way Anova with Tukey's correction was used. Normality was assessed by the Shapiro–Wilk test. **g** Representative anti-CD68 stained paraffin sections and quantification of granulomas in the submucosa of 4-month-old mice with the indicated genotypes; (n = 4,6,7 mice/ genotype), Kruskal–Wallis test was used with Dunn's correction. Normality was assessed by the Kolmogorov–Smirnov test. LP Lamina propria, SM Submucosal layer, MP Muscularis propria. Scale bars = 50 μm. Data are presented as mean values ± SEM. Source data are provided as a Source Data file.

role of *Tnfrsf1a*-expressing fibroblasts, especially the telocytes and Pdgfra^{lo}Cd81^{-} subsets, in triggering inflammation in the lamina propria.

To better understand the requirement of *Tnfrsf1a* expression in distinct fibroblast subpopulations, we employed the *Tnfrsf1a*^{cneo} mutant mice, which harbor a conditional gain-of-function allele for TNFR1 receptor. In these mice, *Tnfrsf1a* expression is blocked by a floxed neomycin cassette, but it can be reactivated through Cre-mediated neo excision. *Col6a1*^{cre} driven expression of *Tnfrsf1a* in telocytes and Pdgfra^{lo}Cd81^{-} cells of *Tnf*$^{\Delta ARE}$ mice induced inflammation restricted in the lamina propria that did not extend into the deeper intestinal layers (submucosa and muscularis mucosa) (Fig. 6d). In contrast when *Tnfrsf1a* was expressed by a broader category of fibroblasts subsets, including trophocytes, inflammation extended beyond the lamina propria and reached the submucosa and muscle layer (Fig. 6d). Also, it became evident that submucosal thickness increased significantly only when *Tnfrsf1a* was expressed in all fibroblast subsets, not solely in telocytes and Pdgfra^{lo}Cd81^{-} (Fig. 6e). The enlargement of submucosa in *Tnfrsf1a*$^{Twist2\text{-}ON}$ *Tnf*$^{\Delta ARE}$ mice was accompanied by immune cell infiltration and fibroblast expansion, indicative of the full development of ileitis in these mice (SFig 13c, d). Finally, although the expression of *Tnfrsf1a* in *Col6a1*^{cre} cells promoted the expansion of TLOs (Fig. 6f), its additional expression in trophocytes was necessary for granuloma formation in the inflamed submucosa (Fig. 6g). To rule out the possibility that *Tnfrsf1a* exerts its pathogenic functions through its expression in FRCs (targeted by both Cre lines), we crossed the conditional gain-of-function *Tnfrsf1a*^{cneo} *Tnf*$^{\Delta ARE}$ model with the Ccl19^{cre} line[37], which is specifically expressed in FRCs within PPs and ILFs/TLOs[38]. As expected, the exclusive expression of *Tnfrsf1a* in FRCs was insufficient to induce either ileal inflammation (SFig. 13e) or the aberrant formation of TLOs (SFig. 13f).

Overall, these findings suggest that TNF signaling in telocytes and/or Pdgfra^{lo}Cd81^{-} cells suffices for the development of inflammation in the lamina propria, and the abberant formation of TLOs. However, only when *Tnfrsf1a* was expressed in all fibroblast subsets (including the trophocytes), there was full expansion and progression of ileitis accompanied by the organization of granulomas.

Discussion

Over recent years, various studies have illuminated the previously underestimated cellular and functional diversity within the intestinal microenvironment during inflammation and under diverse treatment regimens in IBD patients[12–14,31]. In addition, animal IBD models, have proven to be invaluable tools for unraveling essential disease-associated mechanisms. Particularly, the *Tnf*$^{\Delta ARE}$ mice, a widely utilized model of CD-like ileitis, played an important role in unambiguously establishing TNF's causal involvement in the inflammatory response of CD[6,7]. This discovery followed the initial approval of a monoclonal antibody targeting TNF for CD patients[39,40]. In this context, comprehending the pivotal cellular actors and molecular pathogenic drivers contributing to the development of *Tnf*$^{\Delta ARE}$ -associated pathology holds potential for the stratification and treatment of CD patients exhibiting TNF-dependent inflammatory engagement of the ileum.

Our study offers valuable insights into the intricate cellular complexity and variability observed in the *Tnf*$^{\Delta ARE}$ ileum. By conducting a comprehensive single-cell resolution analysis of immune and stromal cells residing in the inflamed ileum, we were able to identify specific changes in population distribution as well as significant transcriptional and functional alterations during the development of the disease with relevance to human CD-ileitis. However, we cannot exclude the possibility that other cell subsets, beyond those we focused on and further analyzed, may also be major regulators of disease pathology.

We initially focused on the immune compartment and identified significant transcriptional changes and shifts in cell population abundances within both myeloid and lymphoid cells. Among the various subsets of T cells, noteworthy modifications in gene expression were observed specifically in memory T cells and Th17 cells. While the existence of effector and memory Th17 cells has been recognized in individuals with IBD, our understanding of the gene program changes that occur within these cells during the disease remains limited[18,41]. Particularly, the role of memory T cells in IBD has been a subject of debate[42]. Our findings indicate that memory T-cells adopt similar gene expression profiles as effector cells, suggesting their potential contribution to the pathogenesis of chronic inflammation.

In the myeloid compartment, we observed a substantial expansion of granulocytes. It's worth noting that many human IBD single-cell studies omit granulocytes[12,13] due to challenges arising from the low RNA content and rapid RNA degradation during scRNA-seq process. Our mouse data underscore the significance of granulocytes as a primary source of pro-inflammatory chemokines, including TNF, IL1a, IL1b, and IL23a. Increased infiltration of neutrophils and activation of fibroblasts have previously been correlated with non-response to several treatments through IL-1R signaling in fibroblasts[29]. Our results indicate that even in a TNF-dependent model, IL1R signaling and neutrophil chemoattractants are significantly enriched in diseased fibroblasts, highlighting the important role of TNF in orchestrating fibroblast activation and neutrophil infiltration.

Focusing on the macrophage populations, we identified two distinct monocyte-derived lineages that are enriched in either *Tnf*$^{\Delta ARE}$ or healthy mice. Activated macrophages which were defined as Lyz1^{+}, CD14^{high} macrophages were preferentially localized to the submucosa of inflamed mice and emerged as the primary source of IL-6 family cytokines. The targeting of signaling pathways associated with various IL-6 family ligands holds promise as a therapeutic strategy for IBD, and multiple ongoing clinical trials are exploring this avenue[43,44]. Additionally, there is evidence of ECM-remodeling gene expression in granuloma-associated macrophages across diverse tissues, suggesting a potential localization of these macrophages within the ileal granulomas of *Tnf*$^{\Delta ARE}$ mice[21]. Consequently, IL-6 ligand production may play a role in the formation and function of these macrophage structures during ileal inflammation.

One additional notable finding was the evident expansion of B cells compared to other lymphocytes. This expansion occurs within TLOs, major sites where B cells are segregated during inflammation, forming active germinal centers (GCs) supported by FRC networks. Previous studies have also noted increased TLOs in both IBD patients[45] and *Tnf*$^{\Delta ARE}$ mice[16]. However, the precise role of TLOs in the disease remains a subject of debate[46]. Interestingly, a recent study indicated that depletion of intestinal TLOs led to increased susceptibility to C. rodentium infection[38]. Nevertheless, in our *Tnf*$^{\Delta ARE}$ mice, the absence of TLOs and PPs did not impact the progression of ileitis, consistent with genetic depletion of B cells that did not influence Tnf$^{\Delta ARE}$ pathology[47]. These findings suggest that the expansion of TLOs and B cells is more likely a consequence of inflammation rather than a contributing factor to the onset and progression of the disease. In addition, the abberant number of autocrine and paracrine interactions developed by the FRC/FDC/MRC subsets reported in our analysis propose pathways propably required for the proper organization and function of these ectopically developed lymphoid structures.

Our single-cell analysis prominently underscores the significant remodeling of fibroblast populations during ileitis. Despite their diminished numbers, likely attributed to the shortened and blunted intestinal villi, these fibroblasts appear to adopt a robust pro-inflammatory phenotype, irrespective of their specific subset distinctions. The expansion of inflammatory fibroblasts has been previously recognized by numerous studies involving IBD patients[12–15]. However, these fibroblasts were categorized as a distinct population, not correlating with the homeostatic fibroblast populations. Our analysis demonstrates that the pro-inflammatory fibroblasts associated with

IBD represent activated states of the pre-existing fibroblast populations (telocytes, Pdgfra^{lo}Cd81^{-} cells, and trophocytes) in the *Tnf*$^{\Delta ARE}$ ileum. In addition, we propose that previously identified emerging pro-inflammatory S4 fibroblasts in murine and human IBD[25], likely represent a pre-existing FRC subset that is not abundant under healthy conditions. Cell communication analysis revealed a pronounced propensity for fibroblasts to engage in communication within the intestinal microenvironment, acting as both active senders and receivers. They mainly serve as sources of chemoattractants for various immune cell types and exhibit heightened responsiveness to diverse cytokine signals. Notably, among these signals, TNF signaling stands out as significantly activated in inflamed fibroblast populations, mirroring findings from studies involving human CD patients. The major sources of TNF were identified as granulocytes and activated macrophages. Indeed, previous evidence showcasing the exclusive production of TNF by myeloid cells has demonstrated its sufficiency in inducing ileal inflammation[47]. In a recent study by Thomas et al., myeloid cells were identified as prominent contributors to TNF production during CD[48]. While this study also highlighted T cells as primary TNF sources, our model did not validate this finding, likely due to the inherent heterogeneity seen in CD patients. Finally, the same study highlighted the potential involvement of TNF signaling in fibroblasts by demonstrating high activation of the TNF pathway in intestinal fibroblasts from CD patients, which was reduced following successful anti-TNF treatment[48].

It is widely acknowledged that initial inflammation in patients with CD occurs in the lamina propria and subsequently advances to the submucosa[49]. This process involves the infiltration of immune cells into the submucosal region along with a localized expansion of fibroblasts in that area[50]. The *Tnf*$^{\Delta ARE}$ phenotype serves as a reflection of these specific histological characteristics. We have previously reported the sufficiency of fibroblast-specific TNFR1 to drive intestinal inflammation[34]. Here, we present compelling evidence that distinct fibroblast populations are pivotal in organizing inflammation across different intestinal layers by orchestrating the formation of specific histopathological features. Telocytes and Pdgfra^{lo}Cd81^{-} fibroblasts, located at the top and within the villi, serve as the first responders to changes in the mucosa. Upon activation through TNFR1 signaling, these cells secrete various chemoattractants that drive mucosal inflammation. Notably, this mucosal inflammation alone is sufficient to initiate the formation of TLOs. In support of this, while TLOs are observed in both the lamina propria and submucosa of IBD patients, in *Tnf*$^{\Delta ARE}$ mice, TLOs exhibit a predominantly mucosal localization, which gradually extends deeper into the intestinal wall. In contrast, additional TNFR1 activation in trophocytes facilitates the penetration of inflammation into the submucosa, promoting the organization of granulomas. We cannot disregard the possibility that *Tnfrsf1a* expressed by muscle cells (targeted by Twist2^{cre}) may also be essential for the development of transmural inflammation during later stages of chronic disease. Our study demonstrates that, beyond their shared homeostatic functions[51], diverse intestinal fibroblast populations contribute differentially to the development of IBD. Furthermore, modulating TNF responses by targeting specific fibroblast subsets emerges as a promising strategy to decouple mucosal from submucosal inflammation and prevent its progression to the chronic phase.

Methods

Mice

Tnf$^{\Delta ARE}$[6], *Col6a1*^{cre}[34], *CMV*^{cre}[52], *Ltbr*$^{f/f}$[53], *Tnfrsf1a*$^{f/f}$[54], and *Tnfrsf1a*^{cneo}1[55] strains were described previously. *Twist2*^{cre} (JAX stock #008712)[33], and *R26*$^{mT/mG}$ (JAX stock #007676)[35] reporter mice were obtained from Jackson Laboratory. *Ccl19*^{cre} mice[37] were kindly provided by Dr. Burkhard Ludewig. All mice (*Mus musculus*) were bred and maintained on a C57BL/6J genetic background in the animal facilities of the Biomedical Sciences Research Center "Alexander Fleming" under specific pathogen-free (SPF) conditions. Housing conditions followed a 12-hour light/dark cycle, with room temperature maintained at 21–24 °C and humidity at 50–60. All mice were observed for morbidity and euthanized when needed according to animal welfare. Mice of both sexes were used in all experiments. Control and experimental mice were either littermates and/or co-housed. Experiments were performed in accordance with all current European and national legislation and were approved by the Institutional Committee of Protocol Evaluation in conjunction with the Veterinary Service Management of the Hellenic Republic Prefecture of Attika (1251-10-03-2014, 8448-18-01-2017, 1988-09-04-2019, 383087/26-03-2024). Experimental mice were euthanized by cervical dislocation.

Histology-Histological evaluation of inflammation

The preparation of intestinal swiss rolls has been previously described[56]. Briefly, terminal ileum (6 cm) was dissected and flushed with ice-cold phosphate-buffered saline (PBS), followed by flushing with modified Bouin's fixative (50% ethanol/5% acetic acid in dH_2O). The ileum was then opened longitudinally and rolled around a toothpick. Swiss rolls were carefully released from the toothpick and fixed overnight (O/N) in 10% formalin (VWR, 9713.5000). Paraffin-embedded mouse ileal swiss rolls were sectioned and stained with haematoxylin and eosin (H&E) and Sirius Red (Sigma, 365548). H&E stained ileal sections were evaluated in a blinded, semiquantitative manner to assess inflammation development across different layers of the intestine. The evaluation was based on the following scale (total: 0-13). Lamina propria: Inflammation scale of 0-4 and expansion scale of 0-1 across the 6 cm of ileum. Submucosa: Inflammation scale of 0-4 and expansion scale of 0-1 across the 6 cm of ileum. Muscularis propria: Inflammation scale of 0-2 and expansion scale of 0-1 across the 6 cm of ileum.

Measurement of submucosal thickness

Submucosal thickness was measured using OlyVIA (Ver.2.9.1) software in whole swiss roll images acquired with an Olympus Slide Scanner VS200 (20X lens). Measurements were made between the muscularis mucosa and the highest myocytes within the circumferential smooth muscle. 30-60 measurements from different ileal areas were taken and averaged for each mouse to provide a direct comparison of submucosal thickness.

Immunofluoresence/Immunohisctochemistry

Ileum (6 cm) was fixed with 4% Paraformaldehyde (PanReac Applichem, A3813)(O/N). Ileal cryosections of 12 μm thickness were rehydrated in wash buffer (0.1% saponin in PBS) for 15 min and blocked in PBS containing 1% albumin (Fisher Scientific, A/1278/46) for 1 h. Sections were incubated with the following primary antibodies: anti-CD45 (AF114, R&D Systems), Biotin-conjugated anti-podoplanin (127403, Biolegend), anti-CD68 (PAS-78996, ThermoFisher) and anti-Pdgfra (AF1062, R&D Systems). Unconjugated antibodies were detected with the following secondary antibodies: Alexa Fluor® 647 goat anti-rabbit (A21244, ThermoFisher) and Alexa Fluor® 647 donkey anti-goat (A21247, ThermoFisher). Biotinylated antibodies were detected using Alexa Fluor® 647 -Streptavidin (S21374, ThermoFisher) and Alexa Fluor® 488-Streptavidin (S32354, ThermoFisher).

For paraffin sections (4 μmthickness), antigen retrieval was performed using Sodium Citrate Buffer (10 mM Sodium Citrate Sigma, S4641, 0.05% Tween 20-Fisher Scientific, BP337-500, pH 6.0) with microwave heating. Tissue permeabilization was achieved with 0.03% Triton X-100 (Acros Organics, 2156825000) in PBS for 10 minutes, followed by blocking in PBS containing 1% albumin for 1 h. Immunofluorescence staining on these sections involved primary antibodies against anti-CD45 (AF114, R&D Systems), Biotin-conjugated anti-podoplanin (127403, Biolegend), anti-CD68 (PAS-78996, ThermoFisher), and anti-collagen IV (ab6586, Abcam). Secondary antibodies,

including Alexa Fluor® 647 goat anti-rabbit (A21244, ThermoFisher), Alexa Fluor® 488 Donkey anti-Rabbit (A21206, ThermoFisher), and Alexa Fluor® 647 donkey anti-goat (A21247, ThermoFisher), were used for signal detection.

Single-cell suspensions from the ileum were concentrated onto slides using a Cytospin™ Centrifuge. The slides were fixed with methanol, permeabilized with 0.1% saponin in PBS, and blocked with PBS containing 1% albumin. They were then incubated with primary antibodies: eFluor™ 660 anti-CD68 (50-0681-82, eBioscience) and anti-Lysozyme EC 3.2.1.17 (A0099, Dako). The secondary antibody used for the detection of Lysozyme was Alexa Fluor® 488 goat anti-rabbit (A11008, ThermoFisher).

Stained sections were mounted with Fluoroshield with DAPI (F6057, Sigma). Imaging was performed using a TCS SP8X White Light Laser confocal system (Leica), a Zeiss LSM900 confocal microscope, and an Olympus Slide Scanner VS200.

Flow cytometry

The isolation of cells from small intestine lamina propria was performed as previously described[36]. In summary, the terminal ileum (6 cm length) was prepared by removing Peyer's patches. The intestine was longitudinally opened and subjected to a 30-minute incubation at 37 °C in HBSS (14170-088, Gibco) containing 5 mM EDTA, DTT (D9779, Sigma), and 10 mM Hepes (LM-S2030, Biosera). After thorough agitation and PBS washes to eliminate epithelial cells, the remaining tissue underwent digestion using 300 U/ml Collagenase XI (C7657, Sigma), 0.08 U/ml Dispase II (18538700, Roche), and 50 U/ml Dnase I (DN25, Sigma) for 40–60 minutes at 37 °C. The resulting cell suspension was filtered through a 70 μmstrainer, followed by centrifugation and resuspension in FACS buffer (PBS with 2% FBS). For stainings, 1–2 million cells/100 μlwere incubated with the following antibodies: anti-CD11c PeCy7 (117318, Biolegend), anti-CD11b APC (101212, Biolegend), anti-CD45 Alexa Fluor 700 (103128, Biolegend), anti-CD45 APC-Cy7 (103116, Biolegend), anti-EPCAM APC-Cy7 (118218, Biolegend), anti-Podoplanin PeCy7 (127412, Biolegend), anti-CD31 PerCP/Cyanine5.5 (102420 Biolegend), anti-B220 FITC (103206, Biolegend), anti-IgA PE (12420483, Invitrogen), anti-TCRβ FITC (11-5961-85, eBioscience), anti-CD81 Biotin, (13-0811-81, eBioscience), anti-Pdgfra BV605 (135916, Biolegend), anti- CD11B PE (557397, BD Pharmigen), anti-MHCII BV605 (107639, Biolegend), anti-Ly6G BV786 (740953, BD Pharmigen), anti-CD64 BV421 (139309, Biolegend), anti-CD24 APC/FIRE 750 (101840, Biolegend), anti-CD14 APC (123311, Biolegend) and anti-VCAM1 Alexa Fluor® 647 (Biolegend, 105712). As a secondary staining for anti-CD81, Alexa Fluor® 647 -Streptavidin (S21374, ThermoFisher) was used. For intracellular staining (against IgA) cells were fixed and permeabilized using the Fixation and Permeabilization Buffer Set (88-8824-00, eBioscience), according to manufacturer's instructions. Propidium Iodide (P1304MP, Sigma), DAPI (D1306, Invitrogen), Zombie Aqua Fixable Viabiloty Kit (423101, Biolegend) or the Zombie-NIR Fixable Viability Kit (423105, Biolegend) was used for live-dead cell discrimination. Absolute number quantification was performed using Precision Count Beads (424902, Biolegend). Samples were analyzed using the FACSCanto II flow cytometer (BD), FACs Celesta (BD) or the FACSAria III cell sorter (BD) and the FACSDiva (BD) or FlowJo software (FlowJo, LLC).

Culture of primary ileal immune cells

The isolation of ileal cells from 3-month-old $Tnf^{+/+}$ and $Tnf^{\Delta ARE}$ mice was performed under sterile conditions, following the procedure used for cell preparation for flow cytometry. $CD45^+$ cells were positively selected using Dynabeads™ Biotin Binder (Invitrogen, 11047) and a biotin-conjugated anti-CD45 antibody (Biolegend, 103104), following the manufacturer's instructions.

Isolated cells were seeded and cultured at a concentration of 1×10^6 cells/ml in a round-bottom 96-well plate. Cells were cultured either in RPMI medium enriched with 10% FBS (Gibco, 10270-106), 1% P/S (Gibco, 15140-122), 2% HEPES (LM-S2030, Biosera), 2% L-glutamine (Gibco, 25030-024), and 0.1% β-mercaptoethanol (Gibco, 31350-010), or with conditioned media derived from TNF-prestimulated or unstimulated fibroblasts.

Supernatants or cell pellets were collected after 24 h. Cell pellets were preserved in TRI (Trizol) Reagent (MRC, TR 118) for downstream analysis.

Enzyme-linked immunosorbent assay (ELISA)

Secretion of TNF in the culture supernatant was measured using TNF ELISA kit (Invitrogen, 88-7324-88) following the manufacturer's instructions.

Culture of primary ileal fibroblasts

The isolation of fibroblasts was performed under sterile conditions, following the same procedure used for cell preparation for flow cytometry. Fibroblasts were isolated from wild-type mice (2–4 months old) and cultured in DMEM (Gibco, 41966-029) supplemented with 10% FBS (Gibco, 10270-106), 1% P/S (Gibco, 15140-122), 2% HEPES (LM-S2030, Biosera), 1% Amphotericin B (Gibco, 1529-0018), 1% L-glutamine (Gibco, 25030-024), and 1% MEM non-essential amino acids (MEM NEAA, Biowest, X0557-100).

At passage 3 (P3), fibroblasts were seeded at a density of 2.5×10^5 cells/ml and stimulated with 10 ng/ml TNF (Peprotech, 315-01 A) for 16 h. Following this, the DMEM medium was replaced with RPMI medium enriched with 10% FBS (Gibco, 10270-106), 1% P/S (Gibco, 15140-122), 2% HEPES (LM-S2030, Biosera), 2% L-glutamine (Gibco, 25030-024), and 0.1% β-mercaptoethanol (Gibco, 31350-010) to facilitate the transfer of conditioned media to immune cells. Supernatants were collected after 24 h.

Additionally, P3 fibroblasts seeded at a density of 250,000 cells/ml were stimulated with conditioned media derived from cultured immune cells isolated from the ileum of $Tnf^{+/+}$ and $Tnf^{\Delta ARE}$ mice.

Migration assay

The isolation of ileal cells from 3-month-old $Tnf^{+/+}$ and $Tnf^{\Delta ARE}$ mice was performed under sterile conditions, following the procedure used for cell preparation for flow cytometry. $CD11B^+$ cells were positively selected using Dynabeads™ Biotin Binder (Invitrogen, 11047) and a biotin-conjugated anti-CD11B antibody (eBioscience, 13-0112-75), according to the manufacturer's instructions.

A total of 250,000 $CD11B^+$ cells were seeded onto Transwell inserts with 3 μm pores (353492, Corning) at a density of 1×10^6 cells/ml in a 24-well plate. The bottom chamber was filled with 750 μl of RPMI or conditioned medium from cultured fibroblasts. After 16 hours, cells that had migrated to the lower chamber were stained with Trypan Blue (Invitrogen, T1082) and live cells were counted using the automated Countess 3 FL (Invitrogen).

Real-time quantitative PCR analysis (qRT-PCR)

Total RNA from cells was purified using the TRI (Trizol) Reagent (MRC, TR 118) and from sorted cell populations using the Single-Cell Ribonucleic Acid Purification Kit (Norgen, 51800). cDNA was synthesized using the Moloney Murine Leukemia Virus Reverse Transcriptase, (M-MLV, Promega, M5313). Real-time polymerase chain reaction was performed in the CFX96 Real-Time System (Bio-Rad) according to the manufacturer's instructions, using the SYBR Select Master Mix (Applied Biosystems, 4472908). Relative gene expression was determined using the $2^{-\Delta\Delta CT}$ method and the primer sequences using in this study were listed as follows: *Ywhaz*-Forward: AGAGTCGTACAAAGACAGCAC, *Ywhaz*-Reverse: GAATGAGGCAGACAAAGGTTG, *Ccl2*-Forward: AGCAC CAGCACCAGCCAACT, *Ccl2*-Reverse: TTCCTTCTTGGGGTCAGCAC, *Cxcl1*-Forward: CCCAAACCGAAGTCATAGCCA and *Cxcl1*-Reverse: CTCCGTTACTTGGGGACACC. *Ywhaz* was used as a housekeeping gene.

Quantification of Granulomas and ILFs/TLOs

Paraffin-embedded histological sections of the terminal ileum (6 cm) were stained with antibodies against CD68 (ThermoFisher, PAS-78996) and B220 (BD Pharmigen, 553084). For the secondary stainings, Biotinylated Rabbit Anti-Rat IgG (Vector, BA-4000) and Biotinylated Goat Anti-Rabbit IgG (Vector, BA-1000) were used, and signal detection and amplification were performed using the ABC kit (Vector Laboratories) with Vectastain DAB (3,3-diaminobenzidine) kit (Vector Laboratories) for signal development, followed by hematoxylin counterstaining.

Slides were visualized using an Olympus Slide Scanner VS200 equipped with a 20× objective lens. ILFs/TLOs were quantified as clusters containing B cells ($B220^+$ cells), while granulomas were identified as macrophage ($CD68^+$) clusters. The numbers of ILFs/TLOs and granulomas were normalized to the total length of the terminal ileum.

ScRNA-seq library preparation and sequencing

FACs sorted intestinal cell populations (150000 cells from each myeloid, lymphoid and stromal subset) from the terminal ileum of 3-month-old $Tnf^{+/+}$ ($n = 2$) and $Tnf^{\Delta ARE}$ ($n = 2$) mice were mixed to an equal ratio and subjected to 10X Chromium Single Cell 3′ Solution v3.1 (target cell recovery 30000 cells/genotype). The scRNA-seq libraries were prepared following the 10X Genomics Single Cell 3′ v3.1 reagent kits pooled and sequenced with the DNBSEQ-G400 sequencer (PE100) (BGI Genomics). The original image data was converted to sequence data via base calling, leading to the storage of raw reads in FASTQ file format. Reads (1,207,791,679 in $Tnf^{+/+}$ sample and 776,706,111 in $Tnf^{\Delta ARE}$ sample) were then aligned to the mouse reference genome (mm10). The steps of read alignment and gene count summarization per cell, were performed using the 10X Genomics Cell Ranger pipeline (v 7.0.1), resulting in 2292 and 2639 median genes detected per cell in $Tnf^{+/+}$ and $Tnf^{\Delta ARE}$ samples respectively.

Sequencing data processing for mouse data

Using the filtered output of cellRanger, we performed a first round of doublet detection running scrublet[57] (v 0.2.3) with default settings in both $Tnf^{\Delta ARE}$ (25,771 cells) and $Tnf^{+/+}$ (43,119 cells) samples. This resulted in the removal of 3063 and 7232 predicted doublets respectively. Next, each sample was processed separately. For both samples low quality cells (genes detected <800 or >7500 and/or percentage of reads mapped to mitochondrial genome >5%) were discarded. Additionally, log-normalization, highly variable genes detection (mean.var.plot, MVP), scaling of the normalized data and PCA analysis ($Tnf^{+/+}$ nPCs: 20, $Tnf^{\Delta ARE\ E}$ nPCs: 22) were executed. Regarding clustering, the Louvain algorithm was employed with a low resolution (res = 0.01) in order to separate the cells in the three major compartments (stroma, lymphoid, myeloid). Following that, three separate objects (one for each compartment) was stored for each sample and subjected to a second round of doublet detection analysis utilizing Doublet Finder[58] package (v 2.0.3) with a doubletRate of 0.046, this resulted in the removal of 1141 WT and 942 DARE cells predicted as doublets. After, integration (Seurat[59] default settings: variance stabilizing transformation VST, canonical correlation analysisCCA) was performed for stroma cells (nPCs = 23, res = 0.5), myeloid (nPCs = 20, res = 0.5) and lymphoid (nPCs = 15, res = 0.5) cells between $Tnf^{+/+}$ and $Tnf^{\Delta ARE}$ samples. Cluster annotation was based on the marker genes, which were calculated using the FindAllMarkers function (Wilcoxon rank sum test, p-value < 0.01, average log(FC) > 0.25, min.pct>0.25) from Seurat package (v 4.3.0). In lymphoid, myeloid and stromal compartments clusters with mixed expression profiles that indicate potential doublets were excluded from downstream analysis, and reclustering of the remaining cells was performed with resolutions 0.4, 0.7, and 0.5, respectively. Differential expression analysis between diseased and healthy conditions, across all clusters, was performed using the FindMarkers function (Wilcoxon rank sum test, p-value < 0.01, absolute average log(FC) > 0.25, and min.pct = 0.1). All the above steps of the analysis (unless mentioned otherwise) were also conducted through the Seurat package. Moreover, to showcase the differential abundance of cell clusters between samples we used contour plots through the package scDataViz[60] (v 1.6.0). For data exploration purposes (expression of genes or gene signatures across clusters) we utilized SCALA (v1.0.0)[61]. Finally, for the visualization of scatter plots, dot plots, violin plots, barplots, venn diagrams and heatmaps the following packages were employed: ggplot2[62] v 3.4.4, Scillus[63] v 0.5.0, dittoseq[64] v 1.8.1, BioVenn[65] v 1.1.3, pheatmap[66] 1.0.12.

Pathway analysis

Overrepresentation analysis (ORA), pathway activity analysis and Single Sample Gene Set Enrichment Analysis (ssGSEA) was performed using metascape (https://metascape.org/), PROGENy (v 1.18.0), decoupleR[67] (v 2.5.2), and scGSVA[68] (v 0.0.22) respectively. Metascape: for stroma, myeloid and lymphoid compartments intra-cluster ($Tnf^{\Delta ARE}$ vs $Tnf^{+/+}$) up/down regulated gene lists from all clusters were used as an input. For the lymphoid compartment positive marker genes were also used to find enriched terms in the different subsets. Additionally, a background genelist was used, considering as active genes all the genes expressed in more than 3 cells. One-tailed hypergeometric test was utilised in metascape and the functional terms returned as an output had a p-value < 0.01, enrichment factor > 1.5 and gene count > 2. Additionally, all selected terms shown in dotplots or heatmaps have also an adj. P-value < 0.01 at least in one cluster. Regarding the network representation in Fig. 1h, i enriched terms are grouped by Metascape into broad functional categories based on gene membership similarity metrics. The term used to describe the category is the one with the highest statistical significance.

ssGSEA: we stratified an alternative approach of GSEA, modified to be more suitable for single-cell data, in order to identify enriched functional terms in myeloid and stroma populations. More specifically, this methodology was previously described[69] and it is offered for single-cell datasets in the R package scGSVA. This method calculates enrichment scores at the single-cell level by ranking genes in each cell according to their expression levels and then using empirical cumulative distribution functions (ECDFs) to compare the set of genes within a given functional term to the set of genes outside the term. To ensure comparability across cells, enrichment scores are normalized by scaling them according to the range of scores across all samples (in our case cells). Furthermore, we calculated z-scores of the normalized enrichment scores (NES) for all cells and gene sets using the ScaleData() function in the Seurat package. These Z-scores were then averaged per cluster, and the top 5 terms were selected for display in the heatmaps. Hallmark gene sets were utilized for stroma clusters, while Reactome pathway gene sets were used for myeloid clusters

PROGENy & decoupleR: As regards the pathway activity analysis, decoupleR proposed methodology for PROGENy was adopted, as described in the vignette (organism = mouse, top 100 genes per pathway), for $Tnf^{+/+}$ and $Tnf^{\Delta ARE}$ samples. In more detail, pathway activity values at the single-cell level were calculated using the PROGENy package, which draws on publicly available signaling perturbation data to identify pathway-responsive genes for pathways such as Androgen, EGFR, Estrogen, Hypoxia, JAK-STAT, MAPK, NFκB, PI3K, TGFβ, TNFα, TRAIL, VEGF, WNT, and p53. We used the run_wmean() function from the decoupleR package for these calculations. The resulting pathway activity matrix was then added as a new assay in the Seurat object. Z-scores were subsequently computed using the ScaleData() function of Seurat, and mean pathway activity scores across all pathways were calculated for each cluster and visualised as a heatmap.

Trajectory analysis

In the myeloid compartment, trajectory analysis was performed utilizing the Slingshot package (v 2.4.0). More particularly, umap coordinates and cluster labels were used as input, while the root cluster was

set to Monocytes. The aforementioned analysis was run in both samples, and the identified lineages were reported. For the bar plots in Supplementary Fig. 3e, pseudotime values calculated using Slingshot were divided into 5 bins (Bin 1: early pseudotime; Bin 5: late pseudotime). For each sample, the percentage of cells assigned to each pseudotime bin is shown.

Integration with human and acute DSS datasets

Human ileitis raw counts data and metadata tables were downloaded from https://singlecell.broadinstitute.org/single_cell/study/SCP1884/human-cd-atlas-study-between-colon-and-terminal-ileum. Cells from the terminal ileum were selected and grouped in stroma and lymphoid Seurat objects. Default Seurat analysis was employed; however, the original cell type annotation was kept. After conversion of the genes from human to mouse, integration between human and mouse datasets was performed for lymphoid and stroma compartments, following the default settings in Seurat (CCA, log-normalization, VST for the top 2000 highly variable genes and number of PCs=20 for lymphoid and PCs=22 for stroma). Next, spearman correlation analysis was performed between the different clusters of $Tnf^{\Delta ARE}$ and human inflamed samples using the normalized values from the "integrated" assay for the top highly variable genes. For the myeloid compartment, two gene signatures containing the top 50 marker genes for resident and inflammatory macrophages (ranked by descending average log(Fold Change) values) were retrieved from a previously published dataset (after reanalysis with Seurat workflow)[12]. Signature scoring was performed using UCell (v 2.0.1), cell scores were summarized at cluster level and plotted in violin plots. For the enrichment analysis presented in Fig. 3j, cells were organized into superclusters (Supplementary Data 6). Next, differential expression analysis was performed in both human (Inflamed vs Healthy) and mouse fibroblasts ($Tnf^{\Delta ARE}$ vs $Tnf^{+/+}$). Consequently up and down regulated genes were identified utilizing the findMarkers function from Seurat with the following parameters and thresholds: two-tailed unpaired Wilcoxon rank sum test p-value < 0.05, min.pct > 0.1, absolute average log(Fold Change)) >0.25. Subsequently, up and down regulated lists of genes were given as input to metascape and overrepresentation analysis was performed as described in the section "Pathway analysis".

Regarding the comparative analysis with the acute DSS data presented in Supplementary Fig. 6, we followed the strategy described next. We integrated our data with single-cell data from Kinchen et al.[25]. Initially, we downloaded the normalized data matrices from GEO and reanalyzed the acute DSS dataset. Next, we integrated the four samples: H_2O-treated control, DSS-treated mouse, $Tnf^{+/+}$, and $Tnf^{\Delta ARE}$, using the methodology implemented in the Seurat V4 package (CCA, log-normalization, VST for the top 2000 highly variable genes and number of PCs=20). For both datasets, we focused exclusively on fibroblast populations. Subsequently, we compared differentially expressed genes (DEGs) from the disease versus healthy comparisons across the datasets (two-tailed unpaired Wilcoxon rank sum test, p-value < 0.01, absolute average log(Fold Change) > 0.25, min.pct > 0.1). Finally, up- and downregulated genes from the previous comparisons were used for functional enrichment analysis via Metascape.

Cell-Chat

Cell–cell communication analysis was performed with CellChat package (v 1.5.0) for both $Tnf^{+/+}$ and $Tnf^{\Delta ARE}$ samples using default options. Glial cells were removed prior to analysis, due to the low number of cells. Additionally, the produced cellchat objects were subjected to comparative analysis using default settings. In order to compare the activation of signaling pathways between the two conditions, netP tables from cellchat objects were utilized and the aggregated probability scores were calculated in two scenarios. In the first non-FRCs fibroblasts (trophocytes, telocytes, $Pdgfra^{lo}Cd81^{-}$) were used as senders and in the second one as receivers. Since communication probability in Cellchat signifies the interaction strength, we calculated a log2 ratio of communication probabilities for all the pathways, which were present in both samples and visualized them in a dotplot format. For the signaling pathways that were found uniquely either in $Tnf^{+/+}$ or $Tnf^{\Delta ARE}$ we reported the aggregated communication probabilty. The same strategy was also applied for the interactions of Ccl2 and Cxcl1 signaling pathways shown in Supplementary Fig. 11a.

Statistics and reproducibility. All experiments were repeated to obtain the required number of replicates. For imaging analyses, representative images from at least three biological replicates are shown. Normality was assessed using the Shapiro–Wilk and Kolmogorov–Smirnov tests. For normally distributed data, statistical analysis was performed using Student's t test or one- or two-way ANOVA. For non-normally distributed data, non-parametric tests were used, including the Mann–Whitney, Kruskal–Wallis, and Wilcoxon tests.

Reporting summary

Further information on research design is available in the Nature Portfolio Reporting Summary linked to this article.

Data availability

The raw and processed sequencing data, along with metadata information, presented in this study, have been deposited in the GEO repository under accession code GSE255350. The raw values are available in the Source Data file whenever possible. Source data are provided with this paper. Data files generated during the bioinformatics analysis are available on Zenodo under the accession code 14860739. External datasets used during the analysis: 1) (Kinchen et al., Cell[25]) acute DSS mouse data were downloaded from GEO under the accession code GSE114374 2) (Kong et al., Immunity, 2023) CD human data were downloaded from Single Cell PORTAL under the accession code SCP1884 3) (Martin et al., Cell, 2019) CD human data were downloaded from GEO under the accession code GSE134809. Source data are provided with this paper.

Code availability

The bioinformatics analysis code and the scripts used for generating the figure plots are available at a dedicated GitHub repository that can be accessed through the following link [https://github.com/ChrisTzaferis/Iliopoulou_et_Al_Wt_Dare12wk_sc_analysis] or in Zenodo under the accession code 14860739.

References

1. Lamb, C. A. et al. British Society of Gastroenterology consensus guidelines on the management of inflammatory bowel disease in adults. *Gut* **68**, s1–s106 (2019).
2. Odze, R. Diagnostic problems and advances in inflammatory bowel disease. *Mod. Pathol.* **16**, 347–358 (2003).
3. Hendrickson, B. A., Gokhale, R. & Cho, J. H. Clinical aspects and pathophysiology of inflammatory bowel disease. *Clin. Microbiol. Rev.* **15**, 79–94 (2002).
4. Derkx, B. et al. Tumour-necrosis-factor antibody treatment in Crohn's disease. *Lancet (Lond., Engl.)* **342**, 173–174 (1993).
5. Levin, A. D., Wildenberg, M. E. & van den Brink, G. R. Mechanism of action of anti-TNF therapy in inflammatory bowel disease. *J. Crohn's. Colitis* **10**, 989–997 (2016).
6. Kontoyiannis, D., Pasparakis, M., Pizarro, T. T., Cominelli, F. & Kollias, G. Impaired on/off regulation of TNF biosynthesis in mice lacking TNF AU- rich elements: Implications for joint and gut-associated immunopathologies. *Immunity* **10**, 387–398 (1999).
7. Iliopoulou, L. & Kollias, G. Harnessing murine models of Crohn's disease ileitis to advance concepts of pathophysiology and treatment. *Mucosal Immunol.* **27**, 1–17 (2021).

8. Zaeem, C. M. & Kaser, A. Recent advances in inflammatory bowel disease: mucosal immune cells in intestinal inflammation. *Gut* **62**, 1653–1664 (2013).
9. Barnhoorn, M. C. et al. Stromal Cells in the Pathogenesis of Inflammatory Bowel Disease. *J. Crohns Colitis* **14**, 995 (2020).
10. Corridoni, D., Chapman, T., Antanaviciute, A., Satsangi, J. & Simmons, A. Inflammatory bowel disease through the lens of single-cell RNA-seq technologies. *Inflamm. Bowel Dis.* **26**, 1658–1668 (2020).
11. Koliaraki, V., Prados, A., Armaka, M. & Kollias, G. The mesenchymal context in inflammation, immunity and cancer. *Nat, Immunol.* **21**, 974–982 (2020).
12. Martin, J. C. et al. Single-cell analysis of Crohn's disease lesions identifies a pathogenic cellular module associated with resistance to anti-TNF therapy. *Cell* **178**, 1493–1508.e20 (2019).
13. Smillie, C. S. et al. Cellular and inter-cellular rewiring of the human colon during ulcerative colitis. *Cell* **178**, 714 (2019).
14. Elmentaite, R. et al. Single-cell sequencing of developing human gut reveals transcriptional links to childhood Crohn's disease. *Dev Cell*. **55**, 771–783.e5 (2020).
15. Korsunsky, I. et al. Cross-tissue, single-cell stromal atlas identifies shared pathological fibroblast phenotypes in four chronic inflammatory diseases. *Med* **3**, 481 (2022).
16. McNamee, E. N. et al. Ectopic lymphoid tissue alters the chemokine gradient, increases lymphocyte retention and exacerbates murine ileitis. *Gut* **62**, 53–62 (2013).
17. Zhou, Y. et al. Metascape provides a biologist-oriented resource for the analysis of systems-level datasets. *Nat Commun*. **10**, 1523 (2019).
18. Kong, L. et al. The landscape of immune dysregulation in Crohn's disease revealed through single-cell transcriptomic profiling in the ileum and colon. *Immunity* **56**, 444–458.e5 (2023).
19. Bel, S. et al. Paneth cells secrete lysozyme via secretory autophagy during bacterial infection of the intestine. *Science* **357**, 1047 (2017).
20. Street, K. et al. Slingshot: cell lineage and pseudotime inference for single-cell transcriptomics. *BMC Genomics* **19**, 477 (2018).
21. Krausgruber, T. et al. Single-cell and spatial transcriptomics reveal aberrant lymphoid developmental programs driving granuloma formation. *Immunity* **56**, 289–306.e7 (2023).
22. Prados, A., Kollias, G. & Koliaraki, V. CollagenVI-Cre mice: a new tool to target stromal cells in secondary lymphoid organs. *Sci. Rep.* **6**, 1–9 (2016).
23. Steiner, C. A. et al. The TNFΔARE mouse as a model of intestinal fibrosis. *Am. J. Pathol.* **193**, 1013–1028 (2023).
24. Iliopoulou, L., Koliaraki, V., Bamias, G. & Kollias, G. Re-evaluating the conclusions of the study by Steiner et al: insufficient evidence to support TNFΔARE mice as a model of intestinal fibrosis. *Am. J. Pathol.* **194**, 1154–1155 (2024).
25. Kinchen, J. et al. Structural remodeling of the human colonic mesenchyme in inflammatory bowel disease. *Cell* **175**, 372–386 (2018).
26. Schubert, M. et al. Perturbation-response genes reveal signaling footprints in cancer gene expression. *Nat. Commun.* **9**, 1–11 (2018).
27. Jin, S. et al. Inference and analysis of cell-cell communication using CellChat. *Nat. Commun*. **12**, 1–20 (2021).
28. Lütge, M., Pikor, N. B. & Ludewig, B. Differentiation and activation of fibroblastic reticular cells. *Immunol. Rev.* **302**, 32–46 (2021).
29. Friedrich, M. et al. IL-1-driven stromal–neutrophil interactions define a subset of patients with inflammatory bowel disease that does not respond to therapies. *Nat. Med.* **27**, 1970–1981 (2021).
30. Nayar, S. et al. A myeloid-stromal niche and gp130 rescue in NOD2-driven Crohn's disease. *Nature* **593**, 275–281.
31. Thomas, T. et al. A longitudinal single-cell therapeutic atlas of anti-tumour necrosis factor treatment in inflammatory bowel disease. *bioRxiv* https://doi.org/10.1101/2023.05.05.539635 (2023).
32. Roulis, M., Armaka, M., Manoloukos, M., Apostolaki, M. & Kollias, G. Intestinal epithelial cells as producers but not targets of chronic TNF suffice to cause murine Crohn-like pathology. *Proc. Natl Acad. Sci. USA* **108**, 5396–5401 (2011).
33. Šošić, D., Richardson, J. A., Yu, K., Ornitz, D. M. & Olson, E. N. Twist regulates cytokine gene expression through a negative feedback loop that represses NF-κB activity. *Cell* **112**, 169–180 (2003).
34. Armaka, M. et al. Mesenchymal cell targeting by TNF as a common pathogenic principle in chronic inflammatory joint and intestinal diseases. *J. Exp. Med.* **205**, 331–337 (2008).
35. Muzumdar, M. D., Tasic, B., Miyamichi, K., Li, N. & Luo, L. A global double-fluorescent cre reporter mouse. *Genesis* **45**, 593–605 (2007).
36. Melissari, M. T. et al. Col6a1+/CD201+ mesenchymal cells regulate intestinal morphogenesis and homeostasis. *Cell Mol. Life Sci*. **79**, 1 (2021).
37. Chai, Q. et al. Maturation of lymph node fibroblastic reticular cells from myofibroblastic precursors is critical for antiviral immunity. *Immunity* **38**, 1013–1024 (2013).
38. Cheng, H. W. et al. Intestinal fibroblastic reticular cell niches control innate lymphoid cell homeostasis and function. *Nat. Commun.* **13**, 1–12 (2022).
39. Targan, S. R. et al. A short-term study of chimeric monoclonal antibody cA2 to tumor necrosis factor α for Crohn's Disease. *N. Engl. J. Med.* **337**, 1029–1035 (1997).
40. Present, D. H. et al. Infliximab for the treatment of fistulas in patients with Crohn's disease. *N. Engl. J. Med.* **340**, 1398–1405 (1999).
41. Jaeger, N. et al. Single-cell analyses of Crohn's disease tissues reveal intestinal intraepithelial T cells heterogeneity and altered subset distributions. *Nat. Commun.* **12**, 1921 (2021).
42. Casalegno Garduño, R. & Däbritz, J. New insights on CD8+ T cells in inflammatory bowel disease and therapeutic approaches. *Front Immunol.* **12**, 738762 (2021).
43. Nayar, S. et al. A myeloid–stromal niche and gp130 rescue in NOD2-driven Crohn's disease. *Nature* **593**, 275 (2021).
44. Shahini, A. & Shahini, A. Role of interleukin-6-mediated inflammation in the pathogenesis of inflammatory bowel disease: focus on the available therapeutic approaches and gut microbiome. *J. Cell Commun. Signal* **17**, 55 (2023).
45. Sura, R., Colombel, J. F. & Van Kruiningen, H. J. Lymphatics, tertiary lymphoid organs and the granulomas of Crohn's disease: an immunohistochemical study. *Aliment Pharm. Ther.* **33**, 930–939 (2011).
46. McNamee, E. N. & Rivera-Nieves, J. Ectopic tertiary lymphoid tissue in inflammatory bowel disease: protective or provocateur? *Front. Immunol.* **7**, 1 (2016).
47. Kontoyiannis, D. et al. Genetic dissection of the cellular pathways and signaling mechanisms in modeled tumor necrosis factor-induced Crohn's-like inflammatory bowel disease. *J. Exp. Med.* **196**, 1563–1574 (2002).
48. Thomas, T. et al. A longitudinal single-cell atlas of anti-tumour necrosis factor treatment in inflammatory bowel disease. *Nat. Immunol.* **25**, 2152–2165 (2024).
49. Schattenfroh, S., Bartels, M. & Nagel, E. Early morphological changes in Crohn's disease. Transmission electron-microscopic findings and their interpretation: an overview. *Acta Anat. (Basel)* **149**, 237–246 (1994).
50. Alfredsson, J. & Wick, M. J. Mechanism of fibrosis and stricture formation in Crohn's disease. *Scand. J. Immunol.* **92**, e12990 (2020).
51. Brügger, M. D. & Basler, K. The diverse nature of intestinal fibroblasts in development, homeostasis, and disease. *Trends Cell Biol.* **33**, 834–849 (2023).
52. Schwenk, F., Baron, U. & Rajewsky, K. A cre-transgenic mouse strain for the ubiquitous deletion of loxP-flanked gene

segments including deletion in germ cells. *Nucleic Acids Res.* **23**, 5080–5081 (1995).
53. Wimmer, N. et al. Lymphotoxin β receptor activation on macrophages induces cross-tolerance to TLR4 and TLR9 ligands. *J. Immunol.* **188**, 3426–3433 (2012).
54. Van Hauwermeiren, F. et al. Safe TNF-based antitumor therapy following p55TNFR reduction in intestinal epithelium. *J. Clin. Invest.* **123**, 2590–2603 (2013).
55. Victoratos, P. et al. FDC-specific functions of p55TNFR and IKK2 in the development of FDC networks and of antibody responses. *Immunity* **24**, 65–77 (2006).
56. Bialkowska, A. B., Ghaleb, A. M., Nandan, M. O. & Yang, V. W. Improved Swiss-rolling technique for intestinal tissue preparation for immunohistochemical and immunofluorescent analyses. *J. Vis. Exp.* **113**, 54161 (2016).
57. Wolock, S. L., Lopez, R. & Klein, A. M. Scrublet: Computational Identification of Cell Doublets in Single-Cell Transcriptomic Data. *Cell Syst.* **8**, 281–291.e9 (2019).
58. McGinnis, C. S., Murrow, L. M. & Gartner, Z. J. DoubletFinder: Doublet Detection in Single-Cell RNA Sequencing Data Using Artificial Nearest Neighbors. *Cell Syst.* **8**, 329–337.e4 (2019).
59. Stuart, T. et al. Comprehensive Integration of Single-Cell Data. *Cell* **177**, 1888–1902.e21 (2019).
60. Blighe, K. "scDataviz: single cell dataviz and downstream analyses." https://github.com/kevinblighe/scDataviz (2020).
61. Tzaferis, C. et al. SCALA: A complete solution for multimodal analysis of single-cell Next Generation Sequencing data. *Comput. Struct. Biotechnol. J.* **21**, 5382–5393 (2023).
62. Wickham, H. ggplot2: Elegant Graphics for Data Analysis. https://ggplot2.tidyverse.org (Springer-Verlag New York, 2016).
63. Xu, M. & Ge, Z. Scillus: Seurat wrapper package enhancing the processing and visualization of single cell data. https://scillus.netlify.app/ (2021).
64. Bunis, D. G., Andrews, J., Fragiadakis, G. K., Burt, T. D. & Sirota, M. dittoSeq: universal user-friendly single-cell and bulk RNA sequencing visualization toolkit. *Bioinformatics* **36**, 5535–5536 (2021).
65. Hulsen, T., de Vlieg, J. & Alkema, W. BioVenn - a web application for the comparison and visualization of biological lists using area-proportional Venn diagrams. *BMC Genomics* **9**, 488 (2008).
66. Kolde, R. pheatmap: Pretty Heatmaps. R package version 1.0.12, https://CRAN.R-project.org/package=pheatmap (2019).
67. Badia-I-Mompel, P. et al. decoupleR: ensemble of computational methods to infer biological activities from omics data. *Bioinform Adv.* **2**, vbac016 (2022).
68. Guo, K. & Wang, Z. scGSVA: GSVA and UCell signature enrichment analysis for single cell RNA seq. https://github.com/guokai8/scGSVA (2024).
69. Barbie, D. A. et al. Systematic RNA interference reveals that oncogenic KRAS-driven cancers require TBK1. *Nature* **462**, 108–112 (2009).

Acknowledgements

The authors would like to thank Dr. Burkhard Ludewig for providing the *Ccl19*^{cre} mice. The authors would also like to thank Meropi Gennadi, Anna Katevaini and Michalis Meletiou for their excellent technical assistance, and Sofia Grammenoudi for her help in the FACs sorting. Finally, we thank Fleming's Animal House, Flow Cytometry and Genomics Facilities. This project has been funded by Horizon Europe Advanced ERC project BecomingCausal (ERC-2021-ADG, ID# 101055093, GK) and by project Single.Out (ID# 3780, GK) funded by the Hellenic Foundation for Research and Innovation (H.F.R.I.) under the "1st Call for H.F.R.I. Research Projects to support Faculty members and Researchers and the procurement of high-cost research equipment". The authors also acknowledge support of this work by infrastructure projects Infrafrontier GR (MIS 5002135, GK) and pMedGR (MIS 5002802, GK), under the Operational Programme "Competitiveness, Entrepreneurship and Innovation", co-financed by Greece and the EU (European Regional Development Fund - ERDF) under NSRF 2014-2020, as well as by project #6004752 of the Operational Programme "Attica", co-financed by Greece and the EU (ERDF) under NSRF 2021-2027.

Author contributions

L.I., A.P., C.T., and G.K. designed the study and interpreted the experimental results. L.I., C.T., and A.P. performed the experiments and data analysis. F.R. performed the 10X library preparation. V.K. contributed to data interpretation. L.I. wrote the manuscript and prepared the figures with contribution from C.T. G.K. edited and finalized the manuscript. All authors were involved in critically revising the final manuscript.

Competing interests

The authors declare no competing interests.

Additional information

Supplementary information The online version contains supplementary material available at https://doi.org/10.1038/s41467-025-57570-7.

Correspondence and requests for materials should be addressed to George Kollias.

Peer review information *Nature Communications* thanks Syed Ali, Sean Colgan and the other, anonymous, reviewer(s) for their contribution to the peer review of this work. A peer review file is available.